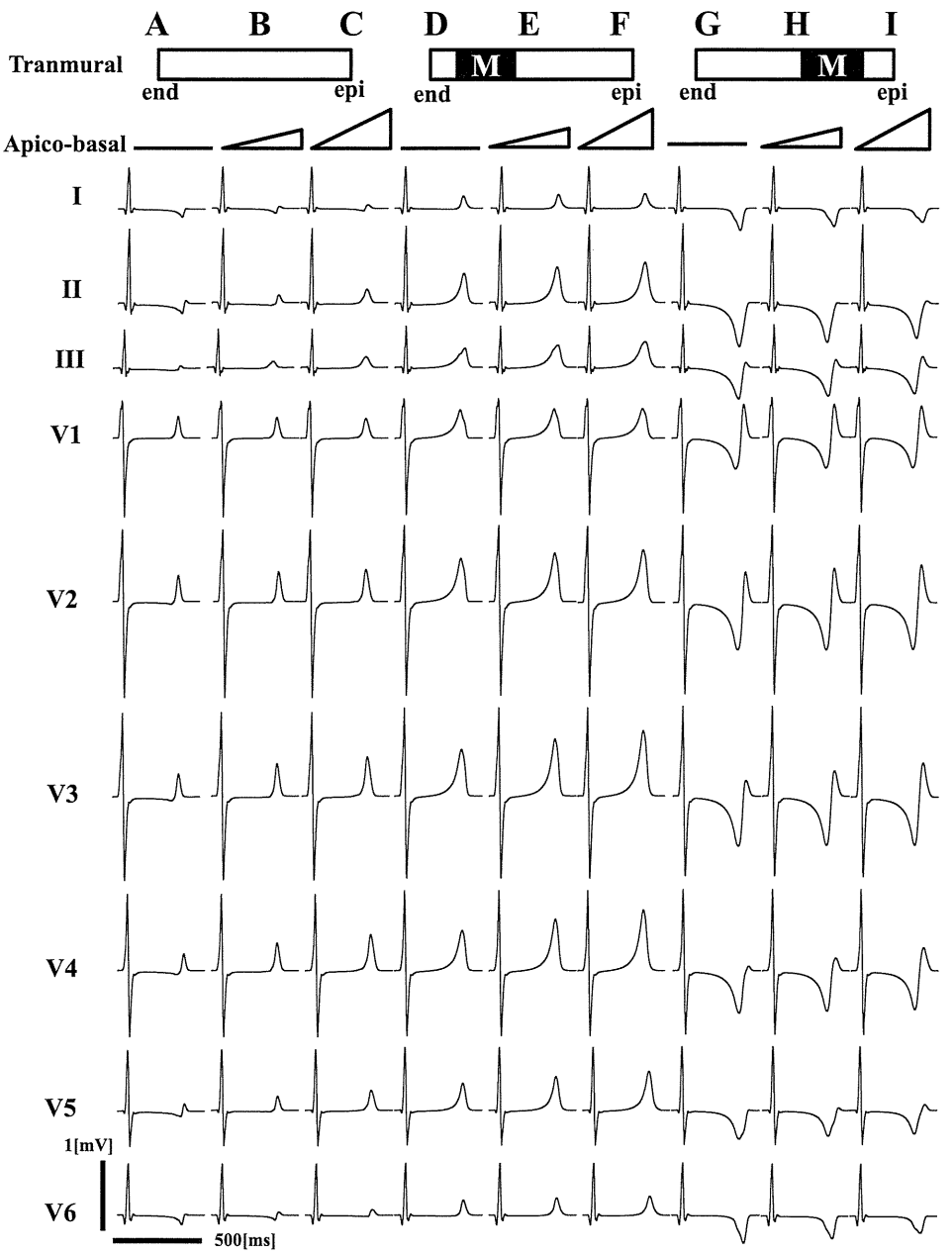

Fig. 4. Electrocardiogram obtained with the nine combinations of the transmural and apicobasal APD gradients. *A*, *B*, and *C* represent the ECGs with no transmural gradient and varying degree of apicobasal gradients. *D*, *E*, and *F* represent the ECGs with M cells on the endocardial side and varying degree of apicobasal gradients. *G*, *H*, and *I* represent the ECGs with M cells on the epicardial side and varying degree of apicobasal gradients.

(*conditions D* and *E*). In healthy subjects, an asymmetry ratio of 1.5 was reported (17), and a correlation between T-wave symmetry and sudden death was suggested. In this regard, we consider that *condition F* may be the most physiological condition for generating a healthy ECG.

Table 1. *Symmetry ratio*

	V2	V3	V4	V5	V6
M cell at endocardium. No apicobasal gradients	1.66	1.74	1.80	1.38	0.70
M cell at endocardium. Apicobasal gradients 20%	1.75	1.76	1.73	1.59	0.94
M cell at endocardium. Apicobasal gradients 40%	1.70	1.70	1.66	1.59	1.02
No M cell. Apicobasal gradients 40%	0.79	0.83	0.96	0.82	0.71

Body surface potential during the repolarization phase. Finally, we compared the body surface potential maps of four conditions (*C*, *D*, *E*, *F*) at the timing of peak T wave, which showed physiological T-wave morphology (Fig. 5) with the previously reported equipotential map of healthy human subjects (39). On the anterior thoracic surface, the positive voltage region of the experimental data (Fig. 3C of Ref. 39) extends down to the lower body, thus resembling *condition F* in our simulation. On the posterior surface, the 0-mV line ran obliquely in the middle of the back so that the positive region was also observed. Taken together, *condition F* showed the closest appearance to the experimental data. The data for different timings can be seen in the Supplemental Movies. Overall, these data suggest that the normal surface ECG waveform cannot be obtained with either transmural or apicobasal gradient of APD alone. Most probably, both contribute to the genesis of surface ECG.

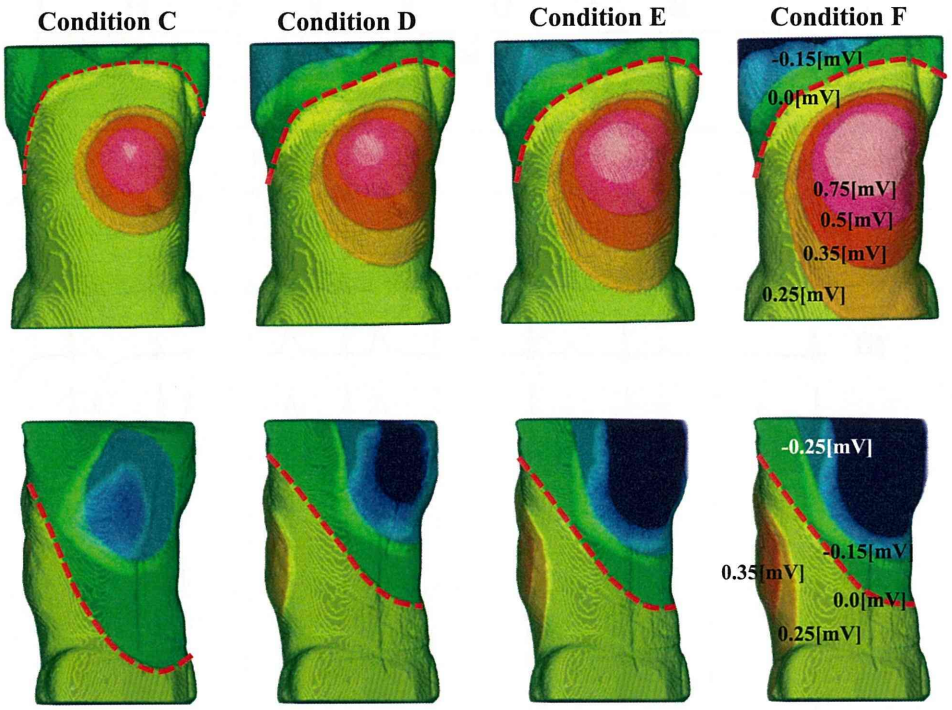

Fig. 5. Body surface potentials at the T-wave peak. *Top* row shows the anterior thoracic surface, and the *bottom* row shows the posterior surface of the results obtained with *models C*, *D*, *E*, and *F*, from *left* to *right*. Red dashed lines indicate the 0-mV line.

DISCUSSION

Computer simulation is a powerful tool in cardiac electrophysiology studies. Various models have been used to examine ECG wave morphology, although studies typically treat either a small number of cell models coupled in series (5, 10, 25) or a tissue block (wedge) (7, 26). Recently, an ionic current model based on large-scale simulation of the heart was developed, although studies using this model are either without the torso (27) or do not examine physiological conduction (52). To the best of our knowledge, this is the first report where surface ECG was simulated based on the ionic current model and anisotropic propagation with the bidomain reaction diffusion equation in a model with realistic morphology of the human torso and heart.

APD dispersion and T-wave morphology. The results of our simulation suggest that the physiological morphologies of T waves are generated mainly by the transmural distribution of APD, although the contribution of the apicobasal gradient is also important. Although recent studies suggest that the cancellation effect in the intact heart can minimize transmural dispersion (5, 41, 42), a large apicobasal gradient is required to observe positive T waves in limb and left precordial leads under such conditions (Fig. 4*C*). Even when using a relatively large apicobasal gradient we could only obtain a highly symmetric, thus nonphysiological, T-wave morphology. Furthermore, the amplitude of the T wave in V6 was very small and symmetric in shape only with the transmural gradient, which is also a nonphysiological morphology.

Recently, experimental evidence of a transmural APD gradient was reported in the human heart (12). However, in contrast to animal data (mainly from electrode recordings), two-dimensional mapping in this study identified M cells clustering in an isolated island, rather than forming a contiguous layer, in 60% of nonfailing ventricular wedge preparations. Furthermore, although the number of samples was limited, that study may suggest the presence of an apicobasal gradient, because these islands were shifted to the basal end in most of the graphs. We simulated the effect of uneven M-cell distribution by reducing the fraction of the M-cell region in the apex. Furthermore, as the data from Glukhov et al. (12) were only taken from a limited region of the left ventricular (LV) wall, we used the smooth apicobasal distribution of M cells and obtained a physiological ECG.

Regional differences. The effect of APD gradient differed among the different leads (see Fig. 6). In the absence of

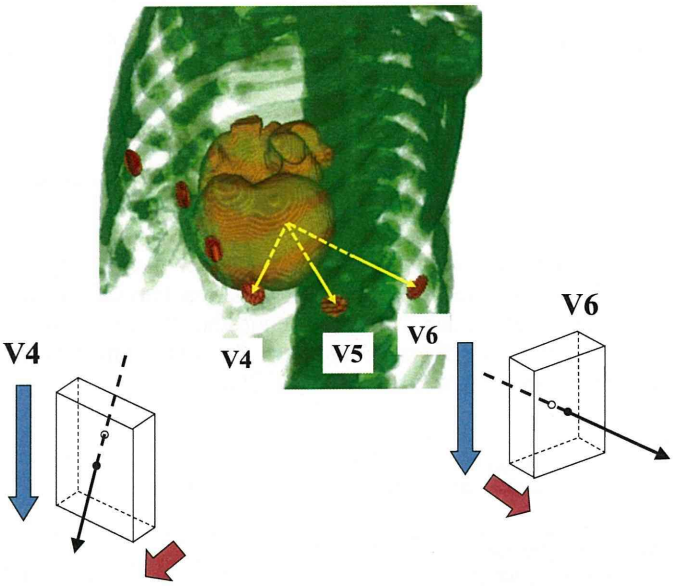

Fig. 6. Diagram showing the effect of lead position on T-wave morphology. The line connecting the V6 lead and the hypothetical zero point crosses the ventricular wall perpendicularly so that the T wave mainly reflects the transverse APD gradient (red arrow). The line connecting the V4 lead and the zero point crosses the wall at an oblique angle so that the T wave is influenced by both transverse (red) and apicobasal gradients (blue arrow).

transmural gradient, the amplitude of the T wave in V6 was small and relatively indifferent to the apicobasal gradient. In a previous study that recorded transmural ECG at 0, 45, −45, and 90° angles relative to the transmural axis, the amplitude of the T wave was highly dependent on the angle and peaked at 0° (53). If we assume that the reference electrode (putative 0 potential) is in the center of the LV, the line connecting this electrode and the V6 lead crosses the LV wall in almost a perpendicular manner and also becomes perpendicular to the apicobasal gradient. On the other hand, because the lines connecting V3 or V4 cross the wall at a shallow angle, T-wave amplitudes are sensitive to the apicobasal gradient. A similar logic may apply to the effect of the transmural gradient when comparing T waves in V5 and V6 among the three conditions without apicobasal gradient. These T waves were either nearly flat, positive, or simply negative (monophasic), thus faithfully reflecting the transmural gradient. Although genesis of surface ECG is not this simple, useful information on APD distribution may be obtained from these comparisons.

Study limitations. Although our simulation faithfully reproduced the physiological ECG waveform, multiple factors needed to be included in our model for further improvement. First, considering the anisotropy in conduction property of the myocardial tissue, the fiber orientation could have a significant impact on the ECG morphology. To examine this possibility, we compared the ECGs obtained with either human (http://gforge.icm.jhu.edu/gf/project/dtmri_data_sets/) or rabbit (30) fiber orientation (Fig. 7) and found no appreciable difference between them. However, as there are numerous reports indicating the deviations of fiber orientation in diseased hearts (13, 16), further studies are required. Second, in this simulation, the APD gradient was introduced by the heterogeneous expression of K^+ channels based on the ad-

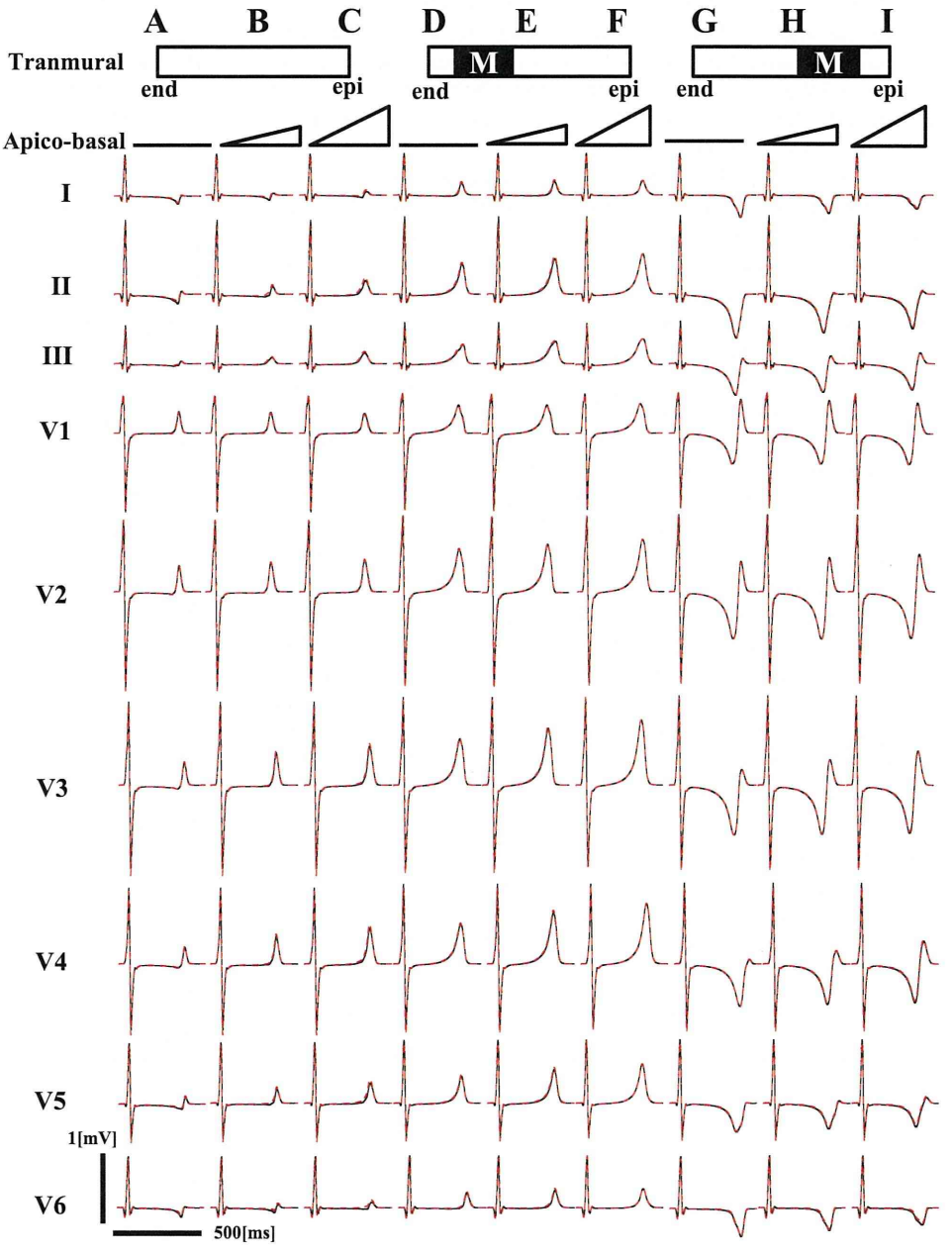

Fig. 7. The ECGs simulated with either human (black line) or rabbit (red line) fiber orientations.

opted cell models (44). However, other molecules are also expressed heterogeneously and thus contribute to the transmural APD gradient. For example, Poelzing et al. (24) reported significantly lower Cx43 expression in the subepicardial layer of the canine LV. Furthermore, downregulation of Cx43 was correlated with the short APD and conduction velocity in this layer. More recently, Poelzing et al. also showed that such heterogeneity in Cx43 expression is significant in anterior LV, and that the poster region lacking Cx43 heterogeneity exhibits flat APD distribution across the wall (37). A similar Cx43 downregulation was reported in the epicardial layer in the human ventricles (12). However, they also showed some discrepancies with the canine heart: *1*) although they studied only the posterior-lateral part of the LV, a significant difference in Cx43 expression was observed transmurally; *2*) although the number of observations was limited, the APD distribution did not show the steep gradient in the epicardial region as shown in the canine heart; and *3*) downregulation of Cx43 in failing human heart resulted in the reduction of local and global transmural APD gradient, thus showing clear contrast to the animal study. Because of these discrepancies between the studies and the lack of information on the whole ventricle, we did not include the effect of Cx43 and only examined effect of the different cell species in our study.

In addition to Cx43, various other ion channels and exchangers are expressed heterogeneously across the ventricular wall. For example, the protein levels of sarco(endo)plasmic reticulum Ca^{2+}-ATPase 2 and ryanodine receptor channel are reduced, whereas the Na/Ca exchanger is upregulated, in the endocardium of the guinea pig ventricle (49). Furthermore, although the number of specimens was small, sarco(endo)plasmic reticulum Ca^{2+}-ATPase 2 mRNA levels were downregulated in endocardial tissue, while Na/Ca exchanger expression was comparable to the epicardial tissue obtained from the human heart (28). Transmural heterogeneity was also reported for the late component of Na currents (29, 54) and the Na-K pump (11). Although APD is influenced by the complex interplay of currents and ion concentrations mediated by these molecules, inclusion of these changes to the model may not drastically change the simulation results, as long as the longer APD is distributed to the endocardial side. Nevertheless, further analysis including these factors is required. Finally, the ST segments in our model appeared to be unusually flat rather than being upslope in some leads. This was likely caused by the flat plateau phase of action potential generated by the ion current model we used (44, 45).

ACKNOWLEDGMENTS

The authors thank Dr. K. Sunagawa (Kyushu University Faculty of Medicine), M. Sugimachi, and Dr. M. Inagaki (National Cardiovascular Center Research Institute) for support in constructing the heart muscle and torso models and for useful suggestions in improving the accuracy of the simulation. The heart simulator used in this study was developed under an intensive research regime supported by Core Research for Evolutional Science and Technology, Japan Science and Technology Agency. The simulator is undergoing continuous development in cooperation with Fujitsu Ltd.

GRANTS

This research is supported by the Japan Science and Technology Agency through its "University-Industry Collaborative Grants Fostering Innovation in Technology-Seeds", and the Japan Society for the Promotion of Science through its "Funding Program for World-Leading Innovative R&D on Science and Technology (FIRST Program)".

DISCLOSURES

No conflicts of interest, financial or otherwise, are declared by the author(s).

REFERENCES

1. **Antzelevitch C.** Transmural dispersion of repolarization and the T wave. *Cardiovasc Res* 50: 426–431, 2001.
2. **Antzelevitch C, Simizu W, Yan GX, Weissenburger J, Nesterenko VV, Burashnikov A, DiDiego JM, Saffitz JE, Thomas GP.** The M cell: its contribution to the ECG and to normal and abnormal electrical function. *J Cardiovasc Electrophysiol* 10: 1124–1152, 1999.
3. **Camacho MA, Lehr JL, Eisenberg SR.** A three-dimensional finite element model of human transthoracic defibrillation: paddle placement and size. *IEEE Trans Biomed Eng* 42: 572–578, 1995.
4. **Conrath CE, Opthof T.** Ventricular repolarization: an overview of (patho)physiology, sympathetic effects and genetic aspects. *Prog Biophys Mol Biol* 92: 269–307, 2006.
5. **Conrath CE, Wilders R, Coronel R, de Bakker JMT, Taggart P, de Groot JR, Opthof T.** Intercellular coupling through gap junctions masks M cells in the human heart. *Cardiovasc Res* 62: 407–414, 2004.
6. **De Ambroggi L, Taccardi B, Macchi E.** Body-surface maps of heart potentials: tentative localization of pre-excited areas in forty-two Wolff-Parkinson-White patients. *Circulation* 54: 251–263, 1976.
7. **Dos Santos RW, Otaviano Campos F, Neumann Ciuffo L, Nygren A, Giles W, Koch H.** ATX-II effects on the apparent location of M cells in a computational model of a human left ventricular wedge. *J Cardiovasc Electrophysiol* 17: S86–S95, 2006.
8. **Drouin E, Charpentier F, Gauthier C, Laurent K, Le Marec H.** Electrophysiologic characteristics of cells spanning the left ventricular wall of human heart: evidence for presence of M cells. *J Am Coll Cardiol* 26: 185–192, 1995.
9. **Durrer D, van Dam RT, Freud GE, Janse MJ, Meijler FL, Arzbaecher RC.** Total excitation of the isolated human heart. *Circulation* 41: 899–912, 1970.
10. **Fish JM, Di Diego JM, Nesterenko V, Antzelevitch C.** Epicardial activation of left ventricular wall prolongs QT interval and transmural dispersion of repolarization implications for biventricular pacing. *Circulation* 109: 2136–2142, 2004.
11. **Gao J, Wang W, Cohen IS, Mathias RT.** Transmural gradients in Na/K pump activity and $[Na^+]I$ in canine ventricle. *Biophys J* 89: 1700–1709 2005.
12. **Glukhov AV, Fedorov VV, Lou Q, Ravikumar VK, Kalish PW, Schuessler RB, Moazami N, Efimov IR.** Transmural dispersion of repolarization in failing and nonfailing human ventricle. *Circ Res* 106: 981–991, 2010.
13. **Helm PA, Younes L, Beg MF, Ennis DB, Leclercq C, Faris OP, McVeigh E, Kass D, Miller MI, Winslow RL.** Evidence of structural remodeling in the dyssynchronous failing heart. *Circ Res* 98: 125–132, 2006.
14. **Henriquez CS.** Simulating the electrical behavior of cardiac tissue using the bidomain model. *Crit Rev Biomed Eng* 21: 1–77, 1993.
15. **Keldermann RH, ten Tusscher KH, Nash MP, Bradley CP, Hren R, Taggart P, Panfilov AV.** A computational study of mother rotor VF in the human ventricles. *Am J Physiol Heart Circ Physiol* 296: H370–H379, 2009.
16. **Maron BJ.** Hypertrophic cardiomyopathy. *Curr Probl Cardiol* 18: 641–704, 1993.
17. **Mirvis DM, Goldberger AL.** Electrocardiography. In: *Heart Disease*, edited by Braunwald E, Zipes DP, and Libby P. Philadelphia, PA: Saunders, 2001, p. 82–125.
18. **Noble D.** From the Hodgkin-Huxley axon to the virtual heart. *J Physiol* 580: 15–22, 2007.
19. **Noble D, Cohen I.** The interpretation of the T wave of the electrocardiogram. *Cardiovasc Res* 12: 13–27, 1978.
20. **Opthof T, Coronel R, Janse MJ.** Is there a significant transmural gradient in repolarization time in the intact heart?: Repolarization gradients in the intact heart. *Circ Arrhythm Electrophysiol* 2: 89–96, 2009.
21. **Panescu D, Webster JG, Tompkins WJ, Stratbucker RA.** Optimization of cardiac defibrillation by three-dimensional finite element modeling of the human thorax. *IEEE Trans Biomed Eng* 42: 185–192, 1995.
22. **Patel C, Burke JF, Patel H, Gupta P, Kowey PR, Antzelevitch C, Yan GX.** Is there a significant transmural gradient in repolarization time in the intact heart?: Cellular basis of the T wave: a century of controversy. *Circ Arrhythm Electrophysiol* 2: 80–88, 2009.

23. **Poelzing S.** Are electrophysiologically distinct M-cells a characteristic of the wedge preparation? *Heart Rhythm* 6: 1035–1037, 2009.
24. **Poelzing S, Akar FG, Baron E, Rosenbaum DS.** Heterogeneous connexin43 expression produces electrophysiological heterogeneities across ventricular wall. *Am J Physiol Heart Circ Physiol* 286: H2001–H2009, 2004.
25. **Potse M, Coronel R, Opthof T, Vinet A.** Simulating T-wave parameters of local extracellular electrograms with a whole-heart bidomain reaction-diffusion model: Size matters! *Conf Proc IEEE Eng Med Biol Soc* 2007: 6644–6647, 2007.
26. **Potse M, Dubé B, Richer J, Vinet A, Gulrajani RM.** A comparison of monodomain and bidomain reaction-diffusion models for action potential propagation in the human heart. *IEEE Trans Biomed Eng* 53: 2425–2435, 2006.
27. **Potse M, Vinet A, Opthof T, Coronel R.** Validation of a simple model for the morphology of the T wave in unipolar electrograms. *Am J Physiol Heart Circ Physiol* 297: H792–H801, 2009.
28. **Prestle J, Dieterich S, Preuss M, Bieligk U, Hasenfuss G.** Heterogeneous transmural gene expression of calcium-handling proteins and natriuretic peptides in the failing human heart. *Cardiovasc Res* 43: 323–331 1999.
29. **Sakmann BFAS, Spindler AJ, Bryant SM, Linz KW, Noble D.** Distribution of a persistent sodium current across the ventricular wall in guinea pig. *Circ Res* 87: 910–914, 2000.
30. **Scollan DF, Holmes A, Winslow R, Forder J.** Histological validation of myocardial microstructure obtained from diffusion tensor magnetic resonance imaging. *Am J Physiol Heart Circ Physiol* 275: H2308–H2318, 1998.
31. **Shimizu W, McMahon B, Antzelevitch C.** Sodium pentobarbital reduces transmural dispersion of repolarization and prevents torsades de Pointes in models of acquired and congenital long QT syndrome. *J Cardiovasc Electrophysiol* 10: 154–164, 1999.
32. **Sicouri S, Antzelevitch C.** A subpopulation of cells with unique electrophysiological properties in the deep subepicardium of the canine ventricle. The M cell. *Circ Res* 68: 1729–1741, 1991.
33. **Sicouri S, Quist M, Antzelevitch C.** Evidence for the presence of M cells in the guinea pig ventricle. *J Cardiovasc Electrophysiol* 7: 503–511, 1996.
34. **Silva JR, Pan H, Wu D, Nekouzadeh A, Decker KF, Cui J, Baker NA, Sept D, Rudy Y.** A multiscale model linking ion-channel molecular dynamics and electrostatics to the cardiac action potential. *Proc Natl Acad Sci USA* 106: 11102–11106, 2009.
35. **Stankovicova T, Szilard M, De Scheerder I, Spido KR.** M cells and transmural heterogeneity of action potential configuration in myocytes from the left ventricular wall of the pig heart. *Cardiovasc Res* 45: 952–960, 2000.
36. **Stewart P, Aslanidi OV, Noble D, Noble PJ, Boyett MR, Zhang H.** Mathematical models of the electrical action potential of Purkinje fibre cells. *Philos Transact A Math Phys Eng Sci* 367: 2225–2255, 2009.
37. **Strom M, Wan X, Poelzing S, Ficker E, Rosenbaum DS.** Gap junction heterogeneity as mechanism for electrophysiologically distinct properties across the ventricular wall. *Am J Physiol Heart Circ Physiol* 298: H787–H794, 2010.
38. **Szentadrassy N, Banyasz T, Biro T, Szabo G, Toth BI, Magyar J, Lazar J, Varro A, Kovacs L, Nanasi PP.** Apico-basal inhomogeneity in distribution of ion channels in canine and human ventricular myocardium. *Cardiovasc Res* 65: 851–860, 2005.
39. **Taccardi B.** Body surface distribution of equipotential lines during atrial depolarization and ventricular repolarization. *Circ Res* 19: 865–878, 1966.
40. **Taccardi B.** Distribution of heart potentials on the thoracic surface of normal human subjects. *Circ Res* 12: 341–352, 1963.
41. **Taggart P, Sutton P, Opthof T, Coronel R, Kallis P.** Electrotonic cancellation of transmural electrical gradients in the left ventricle in man. *Prog Biophys Mol Biol* 82: 243–254, 2003.
42. **Taggart P, Sutton PM, Opthof T, Coronel R, Trimlett R, Pugsley W, Kallis P.** Transmural repolarization in the left ventricle in humans during normoxia and ischaemia. *Cardiovasc Res* 50: 454–462, 2001.
43. **Tawara S.** *Das Reizleitungssystem des Säugetierherzen: Eine anatomisch-histologische Studie uber das Atrioventrikularbundel und die Purkinjeschen Faden.* Jena, Germany: Gustav Fischer, 1906.
44. **Ten Tusscher KH, Noble D, Noble PJ, Panfilov AV.** A model for human ventricular tissue. *Am J Physiol Heart Circ Physiol* 286: H1573–H1589, 2004.
45. **Ten Tusscher KH, Panfilov AV.** Alternans and spiral breakup in a human ventricular tissue model. *Am J Physiol Heart Circ Physiol* 291: H1088–H1100, 2006.
46. **Trayanova NA.** Whole-heart modeling: applications to cardiac electrophysiology and electromechanics. *Circ Res* 108: 113–128, 2011.
47. **Vigmond E, Vadakkumpadan F, Gurev V, Arevalo H, Deo M, Plank G, Trayanova N.** Towards predictive modelling of the electrophysiology of the heart. *Exp Physiol* 94: 563–577, 2009.
48. **Voss F, Opthof T, Marker J, Bauer A, Katus HA, Becker R.** There is no transmural heterogeneity in an index of action potential duration in the canine left ventricle. *Heart Rhythm* 6: 1028–1034, 2009.
49. **Wan X, Laurita KR, Pruvot EJ, Rosenbaum DS.** Molecular correlates of repolarization alternans in cardiac myocytes. *J Mol Cell Cardiol* 39: 419–428, 2005.
50. **Washio T, Okada J, Hisada T.** A parallel multilevel technique for solving the bidomain equation on a human heart with Purkinje fibers and a torso model. *SIAM Review* 52: 717–743, 2010.
51. **Weirich J, Bernhardt R, Loewen N, Wenzel W, Antoni H.** Regional and species-dependent effects of K^+-channel blocking agents on subendocardium and mid wall slices of human, rabbit and guinea pig myocardium (Abstract). *Pflügers Arch* 431: R130, 1996.
52. **Xue J, Gao W, Chen Y, Han X.** Study of repolarization heterogeneity and electrocardiographic morphology with a modeling approach. *J Electrocardiol* 41: 581–587, 2008.
53. **Yan GX, Antzelevitch C.** Cellular basis for the normal t wave and the electrocardiographic manifestations of the long-QT syndrome. *Circulation* 98: 1928–1936, 1998.
54. **Zygmunt AC, Eddlestone GT, Thomas GP, Nesterenko VV, Antzelevitch C.** Larger late sodium conductance in M cells contrbutes to electrical heterogeneity in canine ventricle. *Am J Physiol Heart Circ Physiol* 281: H689–H697, 2001.

Biophysical Journal Volume 101 December 2011 2601–2610

A Three-Dimensional Simulation Model of Cardiomyocyte Integrating Excitation-Contraction Coupling and Metabolism

Asuka Hatano,* Jun-ichi Okada, Takumi Washio, Toshiaki Hisada, and Seiryo Sugiura
Department of Frontier Science, The University of Tokyo, Kashiwa, Chiba, Japan

ABSTRACT Recent studies have revealed that Ca^{2+} not only regulates the contraction of cardiomyocytes, but can also function as a signaling agent to stimulate ATP production by the mitochondria. However, the spatiotemporal resolution of current experimental techniques limits our investigative capacity to understand this phenomenon. Here, we created a detailed three-dimensional (3D) cardiomyocyte model to study the subcellular regulatory mechanisms of myocardial energetics. The 3D cardiomyocyte model was based on the finite-element method, with detailed subcellular structures reproduced, and it included all elementary processes involved in cardiomyocyte electrophysiology, contraction, and ATP metabolism localized to specific loci. The simulation results were found to be reproducible and consistent with experimental data regarding the spatiotemporal pattern of cytosolic, intrasarcoplasmic-reticulum, and mitochondrial changes in Ca^{2+}; as well as changes in metabolite levels. Detailed analysis suggested that although the observed large cytosolic Ca^{2+} gradient facilitated uptake by the mitochondrial Ca^{2+} uniporter to produce cyclic changes in mitochondrial Ca^{2+} near the Z-line region, the average mitochondrial Ca^{2+} changes slowly. We also confirmed the importance of the creatine phosphate shuttle in cardiac energy regulation. In summary, our 3D model provides a powerful tool for the study of cardiac function by overcoming some of the spatiotemporal limitations of current experimental approaches.

INTRODUCTION

In addition to their essential role in supplying energy to the heart, cardiac mitochondria have been observed to take up and release calcium (Ca^{2+}) in cardiomyocytes. However, although the Ca^{2+}-buffering capacity of the mitochondria is potentially significant, its contribution to excitation-contraction coupling through the regulation of cytosolic [Ca^{2+}] has been proven to be negligible (1). Moreover, recent studies have identified further functional significance of mitochondrial Ca^{2+} flux, in that it provides a signal to activate the electron transport chain and ATP synthesis (2,3). Because the change in cytosolic Ca^{2+} concentration also serves as the signal for sarcomere contraction (the primary energy-consuming function of the myocyte), Ca^{2+} flux to the mitochondria may constitute a feed-forward regulatory mechanism for rapid fine-tuning of energy balance within the myocardium. Whether such a feed-forward mechanism is indeed stimulated by the beat-to-beat changes in the mitochondrial calcium concentration (fast Ca^{2+} uptake model) or by integrated changes in cytosolic Ca^{2+} concentration (slow Ca^{2+} uptake model) remains to be determined (4,5).

Prior studies have demonstrated, using Ca^{2+} indicators, that mitochondrial Ca^{2+} concentration changes from beat to beat (6,7); however, the high potential of signal interference from cytosolic Ca^{2+} cannot be excluded in these studies (5,8). On the other hand, where the cytoplasmic Ca^{2+} fluorescence was minimized, both slow (9–11) and fast (12,13) mitochondrial Ca^{2+} uptake has been reported. Recent studies using genetically targeted mitochondrial Ca^{2+} probes reported the occurrence of fast Ca^{2+} uptake by the mitochondria, but with the slow decay of mitochondrial Ca^{2+} still apparent (14,15). Aside from the technical issues involved, research into the mode of mitochondrial Ca^{2+} uptake has demanded important mechanistic considerations. First, whereas the physiological Ca^{2+} transient peaks at 1–2 μmol/L under normal physiological conditions, the half-maximal effective concentration (EC_{50}) of the Ca^{2+} uniporter is reported to be much higher (16,17). Put simply, for the mitochondria to take up a significant amount of Ca^{2+} in this setting, the mitochondria must sense a transient increase in localized [Ca^{2+}] (in the microdomain). To date, the existence of such a microenvironment has been suggested only indirectly or theoretically (13,18,19). Second, because mitochondrial Ca^{2+} cycling dissipates both membrane potential ($\Delta\Psi$) and ΔpH across the mitochondrial inner membrane, additional energy is required for their maintenance. In this sense, it is questionable whether the beat-to-beat adjustment of mitochondrial ATP synthesis to energy demand is cost-effective. Despite the recent advances in equipment and techniques, the current experimental approaches cannot provide us with sufficient resolution with regard to both space and time to resolve these unanswered questions.

Computer simulations are now used for a wide array of applications, facilitating the understanding of complex biochemical and physical processes, including those involved in the bioenergetics of cardiomyocytes (13,20–23). In addition to its potential as an alternative to exhaustive experiments, computer simulation also enables unobstructed observation of biological processes, as well as

Submitted June 14, 2011, and accepted for publication October 11, 2011.

*Correspondence: asuka-h@sml.k.u-tokyo.ac.jp

Editor: Andrew McCulloch.

0006-3495/11/12/2601/10 $2.00

doi: 10.1016/j.bpj.2011.10.020

accurate quantification of the processes occurring beyond the resolution limits of methods currently employed. However, the majority of simulated models constructed to date have primarily focused on the interactions of specific chemical species and elementary processes, with less attention afforded to the geometric aspects of organelle function or the physics underlying Ca^{2+} movement.

We previously developed a three-dimensional (3D) cardiomyocyte model based on the finite-element method, in which the Ca^{2+} wave and resultant contraction were reproducible and authentic (24). The study presented here significantly extends this line of research, enhancing the cardiomyocyte model by adding detailed subcellular structures, including the sarcolemma with t-tubule system, the SR (sarcoplasmic reticulum), the myofibril, and mitochondria. By solving the elementary processes in each organelle, diffusion of Ca^{2+} and energy metabolites, and deformation of the sarcomere induced by active contraction, this model is shown to successfully reproduce changes in cytosolic, intra-SR, and mitochondrial Ca^{2+} during contraction in various inotropic states observed by other experimental methods. Detailed analysis suggests that although the observed large cytosolic Ca^{2+} gradient facilitates uptake by the mitochondrial Ca^{2+} uniporter to produce beat-to-beat changes in mitochondrial Ca^{2+} concentration ($[Ca^{2+}]$) near the Z-line region, the average mitochondrial $[Ca^{2+}]$ changes slowly. We also confirmed the importance of the creatine phosphate shuttle in cardiac energy regulation. Our 3D model of cardiac excitation-contraction and metabolism provides a powerful tool for in-depth analysis of cardiac physiology and function, expanding the temporal and spatial limits of current experimental approaches.

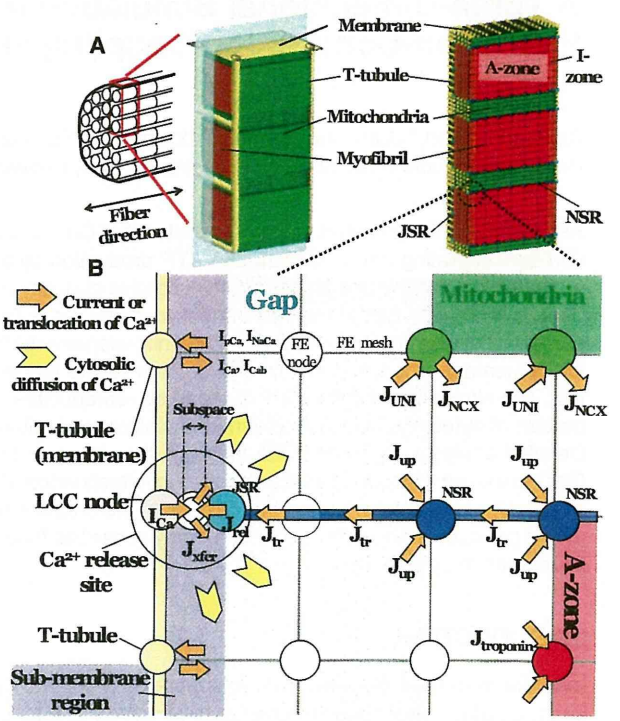

FIGURE 1 (*A*) 3D cardiomyocyte model consisting of three myofibrils of one sarcomere length, including adjacent cell membrane and organelles. The finite-element method was used for modeling. (*B*) Detailed illustration of the model near the t-tubule region including the pathways for Ca^{2+} regulation. J_x represents Ca^{2+} flux by either the uniporter (UNI) or the Na^+-Ca^{2+} exchanger (NCX), uptake by NSR (*up*), release from JSR (*rel*), transfer from NSR to JSR (*tr*), transfer from subspace to cytosol (*xfer*), or binding to troponin C (*troponin*). I_x represents the Ca^{2+} current from the LCC (*Ca*), sarcolemmal Ca^{2+} pump (*pCa*), Na^+-Ca^{2+} exchanger (*NaCa*), or background current (*Cab*). In this region, mesh sizes were made finer for more detailed analysis.

MATERIALS AND METHODS

This model is an extension of our previous 3D cardiomyocyte model (24) to include metabolic processes as well as three features that distinguish it from our earlier model:

1. Detailed subcellular structures, including the sarcolemma with t-tubule system, SR, myofibril, and mitochondria, are reproduced in 3D space, arranged based on published reports.
2. The effect of specific reactions occurring within each functional component (metabolites or ions) able to diffuse across the cytosolic space in 3D, enabling observation of secondary effects at remote loci.
3. The contraction (cross-bridge) model was modified to include the dependence of force generation on metabolite level, sarcomere length, and shortening velocity. Force generation and the resultant deformation of finite elements were repeated to reproduce the true physiological contraction of the myocyte.

The 3D finite-element model of the myocyte

Fig. 1 *A* displays the structure of the 3D myocyte model. To reduce the computational cost, the segment was modeled to contain three myofibrils of one sarcomere length, together with the adjacent cell membrane and organelle. The rationale behind the modeling was that it reproduced longitudinal periodicity and axial symmetry of the myocyte. It was assumed that in a cylindrical myocyte containing 40 myofibrils, three radially arranged myofibrils occupied the space between the cell membrane and the center of the myocyte. At the final stage, further reductions were implemented so that only one-quarter of this model (halved in both length and width) was included for analysis. Such modeling of the small symmetrical segment due to the limited computational power prevented reproduction of local heterogeneity and the axial elements of the t-tubule structure. To overcome this, models were tested in which the t-tubule was partially deleted. Although local deletion of t-tubule induced slight delays in both the upstroke and decay of local Ca^{2+} transients, global behavior of the cell (Ca^{2+} transient, ADP, and SR $[Ca^{2+}]$) was not notably altered (Fig. S5 and Fig. S6 in the Supporting Material). In addition, L-type Ca^{2+} channels (LCCs) are not distributed in the axial elements of t-tubules (25); therefore, omission of the axial element from the model would not significantly affect Ca^{2+} handling. Accordingly, the original model illustrated in Fig. 1 was found to be sufficient and was used subsequently for all simulations. The 3D structure was modeled on a hexahedral solid finite-element model, consisting of 1861 nodes and 581 elements. The total numbers of degrees of freedom were 6164 for mechanical analyses and ~20,000 for physiological simulation. Subcellular components including the mitochondria, myofibril (A-zone, I-zone, and M-line), junctional and network SR (JSR and NSR, respectively), cell membrane, and t-tubules were located at the appropriate nodes to reproduce the anatomical structure and occupy the relative volume (1,26–28). Because the function of each subcellular component was

primarily based on the mathematical formulation proposed by Cortassa et al. (28), modeling of the excitation-contraction coupling of the guinea pig myocyte, the volume ratio of subcellular components (29), and ion channel distribution (30) was also adjusted based on the guinea pig cardiomyocyte. Each subcellular component could exchange ions and/or metabolites into the surrounding cytosol, and these molecules diffused freely through the cytosolic space.

Reaction-diffusion equations

Several investigations of Ca^{2+} dynamics utilizing 3D models have been reported (24). The study described here adopted these formulas for calculating the transport and exchange of metabolites and signaling molecules.

The multiple reaction-diffusion fields for Ca^{2+} and five substrates, including creatine (Cr), creatine phosphate (CP), inorganic phosphate (Pi), adenosine triphosphate (ATP), and adenosine diphosphate (ADP), were defined in the cytosolic space. The reaction-diffusion equations have the x axis in the longitudinal direction, with the z axis in the radial direction, as described below.

At a node where a functional component exists,

$$\frac{d[S]_i}{dt} = \nabla\cdot\left(D_i^s\nabla[S]_i\right) + f_i^s\left(\left[Ca^{2+}\right]_i, [Cr]_i, [CP]_i, [Pi]_i, [ADP]_i, [ATP]_i\right). \quad (1)$$

Alternatively,

$$\frac{d[S]_i}{dt} = \nabla\cdot\left(D_i^s\nabla[S]_i\right). \quad (2)$$

S denotes one of the six substrates, i indicates the location (node), D_i^S is a diagonal matrix describing the diffusivity of substrate S, $[S]_i$ is the concentration of S at position i, and f_i^S is the function describing the reaction of substrate S.

Details of the reaction and diffusion processes near Ca^{2+} release sites are illustrated in Fig. 1 *B*. In this model, the LCC node, JSR node, subspace node, and cytosolic node are colocalized to the Ca^{2+} release site but possess their own Ca^{2+} concentrations for finite-element analysis. The current through the LCC (I_{Ca}) flows into the subspace and activates ryanodine receptors located on the JSR node. Ca^{2+} released from the JSR (J_{rel}) also flows into the subspace and thereafter moves to the cytosolic node to diffuse throughout the entire cytosol. Within the cytosolic space, Ca^{2+} is taken up by the Ca^{2+} uniporter of the mitochondrial node, bound to troponin C in the A-zone thin filament, and sequestered by SERCA2 on the NSR before eventually being transported back to the JSR. Further details outlining the model can be found in the Supporting Material. Similar calculations were performed at each node and for all the ions and metabolites, where pertinent.

Mitochondria and energy metabolism

To incorporate the high EC_{50} of the Ca^{2+} uniporter, we adopted the model proposed by Dash et al. (31). Because mitochondria are exposed to a large cytosolic Ca^{2+} gradient, it was hypothesized that a Ca^{2+} gradient may also exist in the mitochondrial matrix, enabling it to activate the tricarboxylic acid cycle to regionally upregulate NADH and ATP synthesis. To reproduce this process, the reaction-diffusion equation of Ca^{2+} inside the mitochondrial matrix was performed separately considering impermeability of the mitochondrial inner membrane. The exchanges of ions and metabolites between the cytosol and matrix via the inner membrane were mediated by channels and uniporters. The transport of ions and energy metabolites is diagrammed in Fig. S3.

ATP synthesized within the mitochondrial matrix is released into the intermembrane space via the adenine nucleotide translocator (ANT) and transferred to the site of ATP utilization via one of two major pathways, direct diffusion or creatine phosphate (CP) shuttle. In the CP shuttle, ATP is converted to easily diffusible CP by mitochondrial creatine kinase (Mit-CK) localized within the intermembrane space. After diffusion of CP to the site of energy utilization, CP is converted back to ATP through an inverse reaction. The myofibril is the major site of energy utilization, where the ATP regenerating system is localized at the M-line as M-line-bound CK (32). Because no regenerating system exists at the A-zone, I-zone, or Z-line, regenerated ATP diffuses to the A-zone from the M-line. The relative contribution of these two pathways to energy transfer is examined in this study.

Excitation-contraction coupling and myocyte shortening

To establish the link between cross-bridge kinetics and energy metabolism, we adopted the sarcomere model developed by Negroni et al. (33), with a modification made by Matsuoka et al. (34). This model was positioned at each point of the A-zone and generated force depending on the local Ca^{2+} and energy-metabolite concentrations. Using these force values, the mechanical equilibrium was calculated using the finite-element method, assuming hyperelasticity of the material (material properties are listed in Table S2 and Table S3, with validation in Fig. S7 and Fig. S8).

Study protocol

Simulations were performed at 0.5, 1, and 2 Hz. Data obtained at the 200th contraction (pseudo-steady state) were compared. The effect of β-adrenergic stimulation was examined by upregulation of both the LCC (to 125%) and SR Ca^{2+} pump (to 200%) based on prior reports (35,36). The transient response after an abrupt increase in pacing rate from 0.25 to 2 Hz was also examined. The parameters for slow (maximum rate of mitochondrial Ca^{2+} uniporter ($V^{max}{}_{uni}$) = 5.0×10^{-6} mM/ms, maximum rate of mitochondrial NCX ($V^{max}{}_{NCX}$) = 2.0×10^{-5} mM/ms) and fast ($V^{max}{}_{uni} = 2.0 \times 10^{-5}$ mM/ms, $V^{max}{}_{NCX} = 8.0 \times 10^{-5}$ mM/ms) mitochondrial Ca^{2+} handling were applied, and the steady states and transient responses were compared.

Computation

Computation was performed using an Intel Xeon CPU (3.2 GHz) and required 1000 s for a single cycle of 1 Hz contraction. All program codes were written in-house.

RESULTS

Ca^{2+} transients during contraction under steady-state conditions

Changes in $[Ca^{2+}]$, force, and [ADP] during free contractions at 1 Hz are illustrated as time-lapsed 3D images in Fig. 2, with other metabolites and mitochondrial Ca^{2+} illustrated in Fig. S10 and Movie S1. Ca^{2+} released from the JSR attains a high cytosolic concentration at both ends of the sarcomere but fades rapidly via uptake by the NSR as it diffuses toward the M-line (Fig. 2, *left column*). Force generation by the cross-bridges follows the $[Ca^{2+}]$ in the A-zone (Fig. 2, *middle column*). Accumulation of ADP also follows the course of force generation; however, spatial

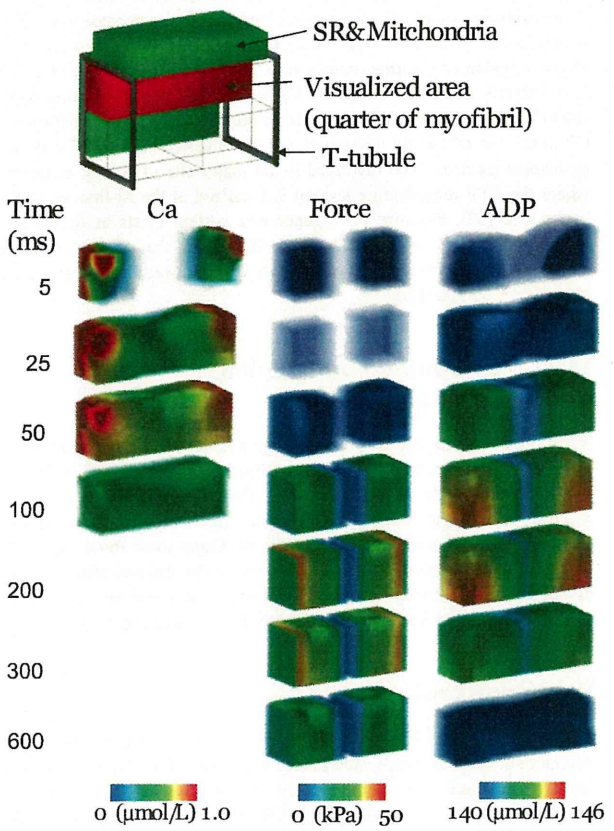

FIGURE 2 Time-lapse images displaying the spatial distribution of [Ca^{2+}], force, and [ADP]. Each panel represents one-quarter of one sarcomere. Numbers on the left indicate time (ms) after the onset of contraction.

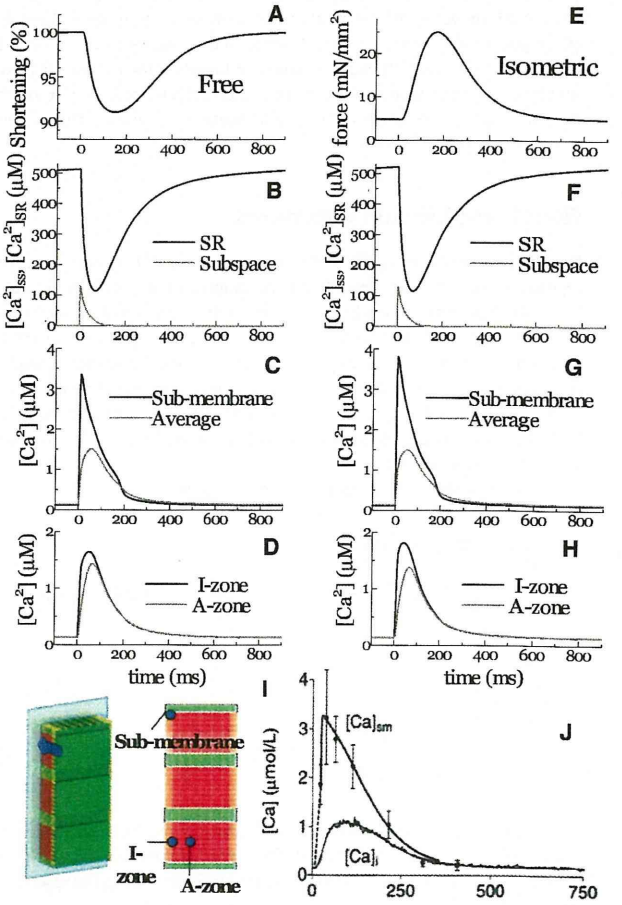

FIGURE 3 Ca^{2+} transients at various loci are displayed in response to changes in length (*A*) or force (*E*) for unloaded (*left column*) and isometric (*right column*) contraction. Ca^{2+} transients were sampled at the SR and the subspace (*B* and *F*), the I-zone and A-zone (*C* and *G*), and the submembrane (*D*) and whole-cytosolic (averaged) regions (*H*). (*I*) Positions referred to in panels C–*H*. (*J*) Experimental data for the submembrane and bulk cytosolic Ca^{2+} transients (reproduced from Weber et al. (37) by copyright permission of the American Heart Association).

distributions were shifted toward the periphery (Z-line) due to the regeneration of ATP at the M-line and an enhanced ATP utilization rate (expressed as the rise in ADP level) caused by the high local [Ca^{2+}] (Fig. 2, *right column*). In this simulation of 1 Hz, sarcomere shortening was found to be 9%. Membrane potential and currents are shown in Fig. S9.

To further examine the spatiotemporal distribution of Ca^{2+} displayed in Fig. 2, local Ca^{2+} signals were sampled at various points in the cytosolic space and SR under both shortening and isometric conditions and plotted with the time course of length and force for each contraction mode (Fig. 3). The beginning of both shortening (Fig. 3 *A*) and isometric (Fig. 3 *E*) contraction was associated with an immediate rise in Ca^{2+} within the subspace (peaking at ~100 μM). This rise coincided with a reduction in SR Ca^{2+} (Fig. 3, *B* and *F*). Ca^{2+} transients in the submembranous space (~20 nm from the t-tubule (Fig. 3 *I*)) were plotted with cytosolic [Ca^{2+}] (Fig. 3, *C* and *G*). Similar to the subspace, submembranous Ca^{2+} transients peaked rapidly, although they only reached ~4 μM, comparable to previous experimental findings (Fig. 3 *J* (37)). Cytosolic [Ca^{2+}] was averaged over the entire model except mitochondrial space, assuming that the experimentally recorded Ca^{2+} signal reflects the fluorescence averaged over the sarcomere. The averaged cytosolic Ca^{2+} transients determined by the current simulation were in agreement with published experimental results (Fig. 3 *J* (37)), supporting the validity of this model. Within the cytosolic space, data were recorded along the center of the sarcomere at two points, 0.1 μm (I-zone) and 0.7 μm (A-zone), respectively, from the Z-line (Fig. 3, *D* and *H*). In the I-zone, the Ca^{2+} transient peak was lower (~1.6 μM) and delayed (~40 ms under free contractions and ~50 ms under isometric conditions) after depolarization. Ca^{2+} peaks at the A-zone were further reduced and delayed (~65 ms) compared to the I-zone under both isometric and free conditions.

Investigating the issue of a fast- or slow-uptake model for mitochondrial Ca^{2+} handling, we compared the simulation

results based on the fast and slow parameter sets with experimental observations (13). For this purpose, mitochondrial and cytosolic Ca^{2+} transients were compared before and after positive inotropic intervention (Fig. 4, *C* and *D* (13)). Positive inotropy was stimulated by upregulation of both the LCC and the SR Ca^{2+} pump. Inotropic intervention increased the peak amplitude of the cytosolic Ca^{2+} transient and accelerated its rapid decay (Fig. 4 *A*, *dashed line*) when compared to control (*solid line*), as reported in the experiment (Fig. 4 *C* (13)). Global mitochondrial Ca^{2+} transients averaged over the entire mitochondrial space increased in amplitude and baseline levels (compare Fig. 4 *B*, *solid* and *dashed lines*) in both fast (*red lines*) and slow (*black lines*) models. The fast model produced greater magnitudes of mitochondrial $[Ca^{2+}]$ compared to the slow model, thus reproducing the experimental results (Fig. 4, *C* and *D*). However, observing the local mitochondrial Ca^{2+} transient near the Ca^{2+} release site under slow model conditions, its amplitude was found to be even larger than under fast model conditions (*blue lines*). Please note that its steep upstroke also resembles the experimental observation.

Transient responses

The responses of $[Ca^{2+}]_{mito}$ and [NADH] to abrupt changes in pacing rate were compared between the simulation presented here (Fig. 5, *A* and *B*) and the experimental results reported by Brandes and Bers in rat trabeculae (Fig. 5, *C* and *D* (38)). Following the experimental protocol of Brandes and Bers (38), the pacing frequency was abruptly

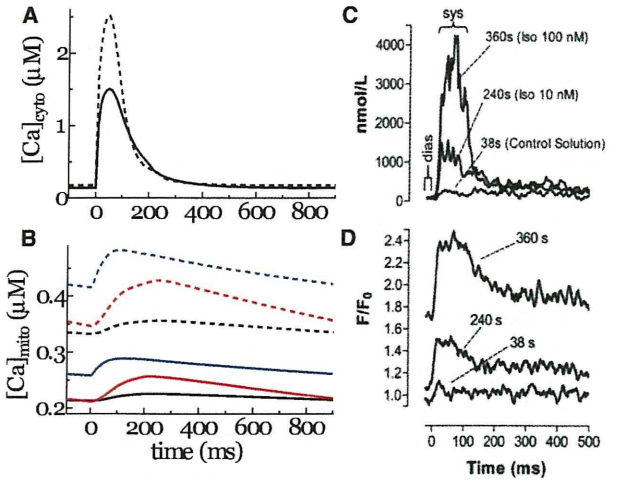

FIGURE 4 (*A* and *B*) Cytosolic (*A*) and mitochondrial (*B*) Ca^{2+} transients subjected to control (*solid line*) or positive inotropic (*dashed line*) conditions. Averaged mitochondrial Ca^{2+} transients under slow (*black line*) and fast (*red line*) parameters for mitochondrial Ca^{2+} handling, and local mitochondrial Ca^{2+} transient under slow parameters are compared in *B*. (*C* and *D*) Prior experimental data for cytosolic (*C*) and mitochondrial (*D*) Ca^{2+} transients from Maack et al. (13) are provided for comparison (by copyright permission of the American Heart Association).

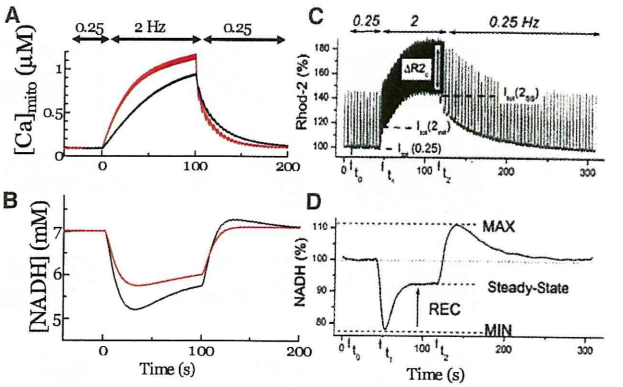

FIGURE 5 Simulated transient response of $[Ca]_{mito}$ (*A*) and [NADH] (*B*) are compared to prior experimental observations of NADH (*C*) and mitochondrial Ca^{2+} (*D*) after an increase in stimulation frequency from 0.25 to 2 Hz in rat cardiac trabeculae (reproduced from Brandes and Bers (38) by copyright permission of the Biophysical Society). Under the simulation model, two sets of parameters, fast (*red line*) and slow (*black line*), are used.

increased from 0.25 Hz to 2 Hz, then relaxed back to 0.25 Hz. Both the fast and slow parameter sets were applied under these conditions, and the results were compared. When subjected to the fast parameters, the change in pacing rate caused a significant increase in mitochondrial Ca^{2+} transient amplitude (Fig. 5 *A*, *red line*). In contrast to the experimental results, the simulation failed to reveal either undershooting or overshooting of NADH (Fig. 5 *B* (*red line*) and *D* (38)). In contrast, under the slow parameters, the NADH response displayed both undershooting and overshooting (Fig. 5 *B*, *black line*), correlating with the rise of mitochondrial Ca^{2+} (Fig. 5 *A*, *black line*), consistent with the experimental results. Taken together, the mitochondrial Ca^{2+} transient produced by our simulation model is consistent with experimental findings only under slow Ca^{2+} handling parameters.

Energy metabolism

Temporal changes in the concentrations of energy metabolites at various loci within the sarcomere were plotted with $[Ca^{2+}]$ at three different pacing rates (Fig. 6 and Fig. S10). The concentration of Ca^{2+} was found to decrease rapidly after peaking near the Z-line with a progressive delay in its peak timing when approaching the M-line (Fig. 6, *top row*). ADP accumulation was found to occur in the Z-line half of the sarcomere, but displayed no delay in its timing (Fig. 6, *second row*). The concentration of creatine increased gradually but homogeneously along the fiber direction due to its high diffusivity (Fig. 6, *third row*). These trends were common to all three pacing conditions tested. In contrast, the response of ANT activity (V_{ANT}) in the mitochondria displayed a unique dependence on the pacing rate (Fig. 6, *bottom row*). At low pacing (0.5 Hz), V_{ANT} peaked at ~100 ms near the Z-line (early peak), with

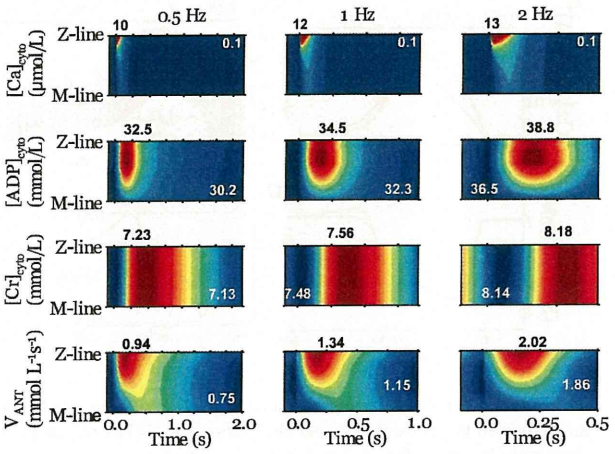

FIGURE 6 Spatiotemporal patterns of (*top to bottom*) $[Ca^{2+}]_{cyto}$, $[ADP]_{cyto}$, $[Cr]_{cyto}$, and ANT exchange velocity. Results for loading of 0.5 Hz (*left column*), 1 Hz (regarded as control) (*middle column*), and 2 Hz (*right column*) are compared. Each panel presents data from half of one sarcomere, with the Z-line at the top and the M-line at the bottom, after each stimulus. Maximum values (*dark red*) are given by black numbers above the panels, and minimum values (*dark blue*) by white letters in the panels.

a less prominent peak also apparent (*yellow green*) at ~400 ms near the M-line (late peak), which coincided with the peak of Cr. The late peak became diminished with increased pacing, and at 2 Hz was no longer evident.

The total amount of ATP synthesis occurring within the sarcomere was compared with the amount converted to CP when subjected to 0.5, 1, or 2 Hz of pacing. The fraction of energy supplied by the CP shuttle system was calculated to be 48.8% (76.1 of 155 μmol L^{-1} s^{-1}) at 0.5 Hz, 47.4% (114 of 241 μmol L^{-1} s^{-1}) at 1 Hz, and 46.5% (183 of 393 μmol L^{-1} s^{-1}) at 2 Hz.

DISCUSSION

An integrated model of cardiomyocyte function

This study employed a 3D cardiomyocyte model in which the electrical, energetic, and mechanical dynamics were integrated with detailed ultrastructures. There have been several previous attempts to develop computational models capable of coupling electrophysiology and Ca^{2+} handling with mitochondrial energetics (28,34); however, because the majority of these models are lumped-parameter models, assuming microcompartments of reaction pools to avoid the computationally challenging partial differential equations, these models only provide us with spatially averaged behavior of ions and metabolites. More intricate models that account for the spatiotemporal pattern of subcellular activities have been developed, but these models have focused only on the transfer of energy metabolites (20,39). To our knowledge, this is the first 3D model to define myocardial energetics coupled with both electrophysiology and Ca^{2+} handling, and to be capable of reproducing the reaction-diffusion phenomena involved in cardiac energy production and utilization. The results obtained using this model go a long way toward explaining some of the controversies currently debated in the field of myocardial energy dynamics, as this model is not subject to the spatiotemporal resolution limitations imposed by current experimental techniques.

Comparison with previous experimental studies

The current simulation model successfully reproduced fundamental contractile characteristics of the cardiac sarcomere. Not only was the average cytosolic $[Ca^{2+}]$ (~1 μM) amplitude and $[Ca]_{SR}$ profile typical of a cardiac sarcomere (Figs. 3, *B* and *F*, and 4, *A* and *C*), but the subcellular distributions and temporal changes of Ca^{2+} were also consistent with previous investigations. For example, Weber et al. (37) estimated the submembrane $[Ca^{2+}]$ ($[Ca^{2+}]_{sm}$), sensed by the Na-Ca exchanger (NCX) by determining the NCX tail current and bulk $[Ca^{2+}]$ ($[Ca^{2+}]_b$) transient. They revealed that the $[Ca^{2+}]_{sm}$ reaches its peak in <32 ms of the action-potential upstroke, and to a level higher than bulk $[Ca^{2+}]$ (Fig. 3 *I*). Consistent with this observation, submembrane $[Ca^{2+}]$ in our simulation was found to peak at 10 ms (~4 μM) (Fig. 3, *C* and *G*). Observing the subspace $[Ca^{2+}]$, no experimental data have been reported to date, although several numerical estimates using detailed diad geometry (40,41) yield values similar to those of the simulation presented here (Fig. 3, *B* and *F*). As for the effect of contraction mode, the peaks of local Ca^{2+} transients under isometric conditions were found to be higher in the submembrane region and I-zone, but reduced in the A-zone compared to the Ca^{2+} transients under free contraction (compare Fig. 3, *C* and *G*, and Fig. 3, *D* and *H*). Furthermore, the time to peak in the I-zone was faster by 10 ms. These differences in Ca^{2+} dynamics observed under different loading conditions are due to the increase in diffusion distance caused by widening of the myocyte; however, we are unaware of any comparable experimental data. On the other hand, the global Ca^{2+} transient did not differ between the isometric and free-contraction modes (compare Fig. 3, *C* and *G*). This finding supports a previous study by White et al. indicating that altering length had no effect on the global Ca^{2+} transient in guinea pig myocytes (42). In contrast, Yasuda et al. reported a significant increase in Ca^{2+} transient peak during shortening contraction in rat ventricular myocytes (43). The cause of this discrepancy remains to be confirmed, but the strain dependence of affinity of Ca^{2+} for troponin C, which we did not incorporate into this model, could be a factor.

Some studies using ^{31}P NMR (44,45) have identified cyclic changes in high-energy phosphate levels (~10%) during the cardiac cycle. However, other studies have found

that cyclical changes are undetectable, or estimated to be only 1.6%, even assuming instantaneous ATP hydrolysis with no resysnthesis (46,47). The reason for this discrepancy is not clear, but as discussed by Illing et al. (44), cyclic changes are mainly found with a high heart rate under crystalline perfusion (inadequate substrate supply) and in vivo large animal studies (low heart rate and blood perfusion) were unable to detect ATP cycling. Our model assumed an adequate substrate supply and reproduced cyclic changes in these metabolites (Fig. 6), but the relative amplitude was small (<1%). Consistent with these results, a simulation study that took into account the effect of high subsarcolemmal Ca^{2+} concentration on the regulation of metabolite concentrations reported even smaller fluctuations (48).

Mitochondrial response

In response to experimentally induced changes in the pacing rate, $[Ca]_{mito}$ is reported to increase or decrease gradually, whereas NADH levels are reported to undershoot and overshoot at the transitions (Fig. 5, *C* and *D*) (38). Our simulation reproduced these responses in $[Ca^{2+}]_{mito}$ and NADH, paralleling the experimental findings over time; however, these effects were only produced under the slow parameters for mitochondrial Ca^{2+} handling (Fig. 5, *A* and *B*). Despite these promising comparative results, the large beat-to-beat oscillations in $[Ca^{2+}]_{mito}$ were not observed in our simulation, nor in the simulation study of Cortassa et al. (28). For the large beat-to-beat oscillations in $[Ca]_{mito}$ to occur, the mitochondrial Ca^{2+} uniporter must encounter high local $[Ca^{2+}]_{cyto}$ due to its high EC_{50}. In addition, a high velocity of mitochondrial Ca transport is required. Because our simulation is comprised of a high submembrane $[Ca^{2+}]_{cyto}$, the fast parameters, i.e., high $V^{uni}{}_{max}$ and high $V^{NCX}{}_{max}$, reproduced the large beat-to-beat $[Ca^{2+}]_{mito}$ oscillations (Fig. 4 *B*, *solid lines*); however, the under- and overshooting of NADH disappeared under fast parameters (Fig. 5 *B*, *red line*). The disparities between our model and prior experimental reports of beat-to-beat $[Ca^{2+}]_{mito}$ oscillations and NADH levels may be explained by the following two possibilities. 1), The experimentally determined fluorescent Ca^{2+} signal may come preferentially from near the Z-line region, where a large transient with steep upstroke can be obtained in our simulation under slow parameters (Fig. 4 *B*, *blue lines*). 2), The disparity may be due to potential errors in modeling the NCX, originating from the controversies of its stoichiometry (49) and K_m dependency on matrix pH (50).

The predicted reductions in cytosolic Ca^{2+} transients due to mitochondrial uptake at 1 Hz were ~2% and 7% under slow and fast mitochondrial Ca^{2+} handling parameters, respectively. Most experimental estimates suggest that this fraction is <~2% (1), supporting the slow model, but one study reported values as high as ~36% (13), which were estimated from large beat-to-beat $[Ca^{2+}]_{mito}$ oscillations. The above discussion may be applied to reconcile such discrepant findings, and in fact, the latter study also suggested that the close proximity of the mitochondria to the Z-line region is the key to realizing a fast response. The authors of that study also performed numerical simulations to reproduce large cyclic changes in $[Ca^{2+}]_{mito}$ by referring to the $[Ca^{2+}]$ in subspace, but metabolic processes were not included in their model.

Finally, it is notable that $[Ca^{2+}]_{mito}$ is not solely governed by the mitochondrial Ca^{2+} uniporter sensing transient high $[Ca^{2+}]_{cyto}$ induced by SR Ca^{2+} release. During the resting phase, Ca^{2+} extrusion by NCX in t-tubules lowers $[Ca^{2+}]_{cyto}$ to near the Z-line region to facilitate the release flux of Ca^{2+} by mitochondrial NCX. In addition, because the actions of the mitochondrial uniporter and NCX are driven by the inner membrane potential, the energetic state also affects mitochondrial Ca^{2+} cycling.

Functional significance of the CP shuttle

Comparison of the findings of spatiotemporal distribution of energy metabolites under different loading conditions suggests the functional significance of CP shuttling. At 0.5 Hz, ANT activity was found to peak at ~100 ms at loci near the Z-line (Fig. 6, *bottom row, left*), which coincides with the peak of ADP (Fig. 6, *second row, left*). Because [ADP] preferentially increases in this region, it is natural to consider that this early peak in ANT activity is induced by the ADP diffusing into the mitochondria. However, we found that the region of high [ADP] is shifted to the I-band rather than to the A-band, where ATP consumption is high (Fig. 6, *second row*, and Fig. 2). This shift in ADP distribution, caused by M-line-bound CK, may be beneficial for force generation, by avoiding the accumulation of ADP around cross-bridges at the A-band. It is interesting that we identified another less prominent peak in V_{ANT} at 400 ms, coinciding with the Cr peak. It appears that this late peak of V_{ANT} may extend toward the Z-line, delaying the decay of ANT activity near the Z-line. Although ANT is not directly activated by Cr, such a spatiotemporal coincidence suggests that the Cr-CP system is capable of modulating mitochondrial activity without raising the ADP level at the A-band.

As the pacing rate was increased, the late V_{ANT} peak became less prominent, and at 2Hz, it had ceased to exist, with only the early peak at ~100 ms (Fig. 6, *bottom row, right*), despite Cr maintaining its delayed peak, as observed under lower loading conditions. Further analysis revealed that the concentration of Cr, even at its nadir, is much greater than the peak value observed under control conditions (Fig. 6, *third row*). We hypothesize that this is likely due to the limited capacity of the mitochondria to maintain the energy balance in response to the excessive amount of ADP produced. This would subsequently cause [Cr] to remain elevated throughout the relaxation phase. Put simply,

the Cr system providing the stimulatory signal for energy production has become saturated. The contribution of the CP shuttle in the energy-transfer process supports this hypothesis, as the absolute contribution of the CP shuttle was found to increase with higher-frequency pacing (from 76.1 μmol L^{-1} s^{-1} under 0.5 Hz to 183 μmol L^{-1} s^{-1} under 2 Hz), although the relative contribution was in fact reduced (from 48.8% under 0.5 Hz to 46.5% under 2 Hz). Our simulation model calculations indicated that the CP shuttle system had a relative contribution of ~50%, comparable to results of a prior experimental study demonstrating that the uncoupling of the CK system lowered the sliding velocity of cardiac myosin by 30% (51). Moreover, Kaasik et al. also reported that ATP directly supplied by the mitochondria was nearly as effective as CK-supplied ATP, and they estimated that 65% of the ATP consumed came from the CK reaction, with the remaining 35% from the mitochondria (52).

Limitations of the model

Because of the current lack of experimental observations of some of the material properties and microscopic structures, this model required the use of estimations and approximations that warrant further explanation. First, in the reaction-diffusion equations, electrical field and convection are not considered to be the source of motive force for the transport of ions and metabolites. Although their contribution is considered to be small compared with that of diffusion, quantitative analyses over a wide range of conditions are required. To model mitochondrial membrane potential, the electric field was ignored, assuming equipotential of the mitochondrial membrane, partly due to the complex folding of its structure. However, we cannot deny the possibility that uneven distribution of ions in the cytosol and/or mitochondrial matrix could create potential gradients, altering ATP synthesis.

Second, diffusion coefficients inside the mitochondrial matrix are controversial. Experimental estimates of matrix diffusivity range from one-third to one-fortieth of that of the cytosol (53,54). Moreover, a prior simulation study reported that the apparent diffusion coefficient of a closed cylinder decreased to half, with 20 diffusion barriers, each occluding 53% of the lumen (55). Preliminary studies were performed in which the diffusivity was varied from one-half to one-thousandth of that of the cytosol, but little difference in energetic balance was detected (data not shown). The lack of change could be partially due to the equipotential assumption of the mitochondrial membrane, but this remains to be confirmed.

The mathematical models for the LCC need improvements to respond to regional variation in Ca^{2+} transients. Because the models currently used are phenomenological in nature and designed to function either in the junction or on the surface of sarcolemma, we needed to use two different models of LCC depending on the range of $[Ca^{2+}]$ they refer. This point is further discussed in Section 3 of the Supporting Material.

Because of the limited computational power, we attempted to examine the role of a general, idealistic arrangement of subcellular structures. However, as suggested by a recent study (56), geometry that is more realistic can change the diffusion distances and affect the predictions of Ca^{2+} and metabolite gradients.

The concept of the CaRU consisting of LCCs and RyRs is supported by the observation of Ca^{2+} sparks (57), but we did not simulate this important phenomenon in our study. Further improvement of the model is required to reproduce such a stochastic process.

SUPPORTING MATERIAL

Four sections, a movie, nine table, 11 figures, and references are available at http://www.biophysj.org/biophysj/supplemental/S0006-3495(11)01239-2.

This research is supported by the Japan Society for the Promotion of Science (JSPS) through its Research Fellowships for Young Scientists (to A.H.) and its Funding Program for World-Leading Innovative R&D on Science and Technology (FIRST) (to A.H., J.O., T.W., S. S., and T.H.), and by JSPS KAKENHI (grant-in-aid) (B) (20300152) (to S.S.). It was also supported by the Japan Science and Technology Agency (JST) through its University-Industry Collaborative Grants Fostering Innovation in Technology-Seeds.

REFERENCES

1. Bers, D. M. 2001. Sources and sinks of activator calcium. *In* Excitation-Contraction Coupling and Cardiac Contractile Force. Kluwer Academic, Dordrecht. 39–56.
2. Balaban, R. S., S. Bose, ..., P. R. Territo. 2003. Role of calcium in metabolic signaling between cardiac sarcoplasmic reticulum and mitochondria in vitro. *Am. J. Physiol. Cell Physiol.* 284:C285–C293.
3. Territo, P. R., V. K. Mootha, ..., R. S. Balaban. 2000. Ca^{2+} activation of heart mitochondrial oxidative phosphorylation: role of the F_0/F_1-ATPase. *Am. J. Physiol. Cell Physiol.* 278:C423–C435.
4. Csordás, G., A. P. Thomas, and G. Hajnóczky. 2001. Calcium signal transmission between ryanodine receptors and mitochondria in cardiac muscle. *Trends Cardiovasc. Med.* 11:269–275.
5. O'Rourke, B., and L. A. Blatter. 2009. Mitochondrial Ca^{2+} uptake: tortoise or hare? *J. Mol. Cell. Cardiol.* 46:767–774.
6. Trollinger, D. R., W. E. Cascio, and J. J. Lemasters. 2000. Mitochondrial calcium transients in adult rabbit cardiac myocytes: inhibition by ruthenium red and artifacts caused by lysosomal loading of Ca^{2+}-indicating fluorophores. *Biophys. J.* 79:39–50.
7. Mackenzie, L., H. L. Roderick, ..., M. D. Bootman. 2004. The spatial pattern of atrial cardiomyocyte calcium signalling modulates contraction. *J. Cell Sci.* 117:6327–6337.
8. Dedkova, E. N., and L. A. Blatter. 2008. Mitochondrial Ca^{2+} and the heart. *Cell Calcium.* 44:77–91.
9. Miyata, H., H. S. Silverman, ..., R. G. Hansford. 1991. Measurement of mitochondrial free Ca^{2+} concentration in living single rat cardiac myocytes. *Am. J. Physiol.* 261:H1123–H1134.
10. Griffiths, E. J., M. D. Stern, and H. S. Silverman. 1997. Measurement of mitochondrial calcium in single living cardiomyocytes by selective removal of cytosolic indo 1. *Am. J. Physiol.* 273:C37–C44.

11. Zhou, Z., M. A. Matlib, and D. M. Bers. 1998. Cytosolic and mitochondrial Ca^{2+} signals in patch clamped mammalian ventricular myocytes. *J. Physiol.* 507:379–403.
12. Griffiths, E. J. 1999. Species dependence of mitochondrial calcium transients during excitation-contraction coupling in isolated cardiomyocytes. *Biochem. Biophys. Res. Commun.* 263:554–559.
13. Maack, C., S. Cortassa, ..., B. O'Rourke. 2006. Elevated cytosolic Na^+ decreases mitochondrial Ca^{2+} uptake during excitation-contraction coupling and impairs energetic adaptation in cardiac myocytes. *Circ. Res.* 99:172–182.
14. Robert, V., P. Gurlini, ..., T. Pozzan. 2001. Beat-to-beat oscillations of mitochondrial $[Ca^{2+}]$ in cardiac cells. *EMBO J.* 20:4998–5007.
15. Bell, C. J., N. A. Bright, ..., E. J. Griffiths. 2006. ATP regulation in adult rat cardiomyocytes: time-resolved decoding of rapid mitochondrial calcium spiking imaged with targeted photoproteins. *J. Biol. Chem.* 281:28058–28067.
16. Gunter, T. E., K. K. Gunter, ..., C. E. Gavin. 1994. Mitochondrial calcium transport: physiological and pathological relevance. *Am. J. Physiol.* 267:C313–C339.
17. Sedova, M., E. N. Dedkova, and L. A. Blatter. 2006. Integration of rapid cytosolic Ca^{2+} signals by mitochondria in cat ventricular myocytes. *Am. J. Physiol. Cell Physiol.* 291:C840–C850.
18. Sharma, V. K., V. Ramesh, ..., S. S. Sheu. 2000. Transport of Ca^{2+} from sarcoplasmic reticulum to mitochondria in rat ventricular myocytes. *J. Bioenerg. Biomembr.* 32:97–104.
19. Belmonte, S., and M. Morad. 2008. 'Pressure-flow'-triggered intracellular Ca^{2+} transients in rat cardiac myocytes: possible mechanisms and role of mitochondria. *J. Physiol.* 586:1379–1397.
20. Aliev, M. K., F. A. van Dorsten, ..., V. A. Saks. 1998. Mathematical model of compartmentalized energy transfer: its use for analysis and interpretation of ^{31}P-NMR studies of isolated heart of creatine kinase deficient mice. *Mol. Cell. Biochem.* 184:209–229.
21. Cortassa, S., M. A. Aon, ..., B. O'Rourke. 2003. An integrated model of cardiac mitochondrial energy metabolism and calcium dynamics. *Biophys. J.* 84:2734–2755.
22. Shannon, T. R., F. Wang, ..., D. M. Bers. 2004. A mathematical treatment of integrated Ca dynamics within the ventricular myocyte. *Biophys. J.* 87:3351–3371.
23. Bazil, J. N., G. T. Buzzard, and A. E. Rundell. 2010. Modeling mitochondrial bioenergetics with integrated volume dynamics. *PLOS Comput. Biol.* 6:e1000632.
24. Okada, J., S. Sugiura, ..., T. Hisada. 2005. Three-dimensional simulation of calcium waves and contraction in cardiomyocytes using the finite element method. *Am. J. Physiol. Cell Physiol.* 288:510–522.
25. Scriven, D. R. L., P. Dan, and E. D. W. Moore. 2000. Distribution of proteins implicated in excitation-contraction coupling in rat ventricular myocytes. *Biophys. J.* 79:2682–2691.
26. Aliev, M. K., P. Dos Santos, ..., V. A. Saks. 2002. Water content and its intracellular distribution in intact and saline perfused rat hearts revisited. *Cardiovasc. Res.* 53:48–58.
27. Chen-Izu, Y., S. L. McCulle, ..., L. T. Izu. 2006. Three-dimensional distribution of ryanodine receptor clusters in cardiac myocytes. *Biophys. J.* 91:1–13.
28. Cortassa, S., M. A. Aon, ..., R. L. Winslow. 2006. A computational model integrating electrophysiology, contraction, and mitochondrial bioenergetics in the ventricular myocyte. *Biophys. J.* 91:1564–1589.
29. Forbes, M. S., and E. E. van Neil. 1988. Membrane systems of guinea pig myocardium: ultrastructure and morphometric studies. *Anat. Rec.* 222:362–379.
30. Pásek, M., J. Simurda, ..., G. Christé. 2008. A model of the guinea-pig ventricular cardiac myocyte incorporating a transverse-axial tubular system. *Prog. Biophys. Mol. Biol.* 96:258–280.
31. Dash, R. K., and D. A. Beard. 2008. Analysis of cardiac mitochondrial Na^+-Ca^{2+} exchanger kinetics with a biophysical model of mitochondrial Ca^{2+} handling suggests a 3:1 stoichiometry. *J. Physiol.* 586:3267–3285.
32. Wegmann, G., E. Zanolla, ..., T. Wallimann. 1992. In situ compartmentation of creatine kinase in intact sarcomeric muscle: the acto-myosin overlap zone as a molecular sieve. *J. Muscle Res. Cell Motil.* 13:420–435.
33. Negroni, J. A., and E. C. Lascano. 1996. A cardiac muscle model relating sarcomere dynamics to calcium kinetics. *J. Mol. Cell. Cardiol.* 28:915–929.
34. Matsuoka, S., N. Sarai, ..., A. Noma. 2004. Simulation of ATP metabolism in cardiac excitation-contraction coupling. *Prog. Biophys. Mol. Biol.* 85:279–299.
35. Brette, F., P. Rodriguez, ..., C. H. Orchard. 2004. β-adrenergic stimulation restores the Ca transient of ventricular myocytes lacking t-tubules. *J. Mol. Cell. Cardiol.* 36:265–275.
36. Brette, F., S. Despa, ..., C. H. Orchard. 2005. Spatiotemporal characteristics of SR Ca^{2+} uptake and release in detubulated rat ventricular myocytes. *J. Mol. Cell. Cardiol.* 39:804–812.
37. Weber, C. R., V. Piacentino, 3rd, ..., D. M. Bers. 2002. Na^+-Ca^{2+} exchange current and submembrane $[Ca^{2+}]$ during the cardiac action potential. *Circ. Res.* 90:182–189.
38. Brandes, R., and D. M. Bers. 2002. Simultaneous measurements of mitochondrial NADH and Ca^{2+} during increased work in intact rat heart trabeculae. *Biophys. J.* 83:587–604.
39. Selivanov, V. A., S. Krause, ..., M. Cascante. 2007. Modeling of spatial metabolite distributions in the cardiac sarcomere. *Biophys. J.* 92:3492–3500.
40. Langer, G. A., and A. Peskoff. 1996. Calcium concentration and movement in the diadic cleft space of the cardiac ventricular cell. *Biophys. J.* 70:1169–1182.
41. Soeller, C., and M. B. Cannell. 1997. Numerical simulation of local calcium movements during L-type calcium channel gating in the cardiac diad. *Biophys. J.* 73:97–111.
42. White, E., M. R. Boyett, and C. H. Orchard. 1995. The effects of mechanical loading and changes of length on single guinea-pig ventricular myocytes. *J. Physiol.* 482:93–107.
43. Yasuda, S., S. Sugiura, ..., H. Sugi. 2003. Unloaded shortening increases peak of Ca^{2+} transients but accelerates their decay in rat single cardiac myocytes. *Am. J. Physiol. Heart Circ. Physiol.* 285:H470–H475.
44. Illing, B., M. Horn, ..., S. Neubauer. 1998. Changes of myocardial high-energy phosphates with the cardiac cycle during acute or chronic myocardial stress. *Magn. Reson. Med.* 40:727–732.
45. Honda, H., K. Tanaka, ..., T. Haneda. 2002. Cyclical changes in high-energy phosphates during the cardiac cycle by pacing-Gated ^{31}P nuclear magnetic resonance. *Circ. J.* 66:80–86.
46. Balaban, R. S., and F. W. Heineman. 1989. Control of mitochondrial respiration in the heart *in vivo*. *Mol. Cell. Biochem.* 89:191–197.
47. Kantor, H. L., R. W. Briggs, ..., R. S. Balaban. 1986. Gated in vivo examination of cardiac metabolites with 31P nuclear magnetic resonance. *Am. J. Physiol.* 251:H171–H175.
48. Michailova, A., and A. McCulloch. 2001. Model study of ATP and ADP buffering, transport of Ca^{2+} and Mg^{2+}, and regulation of ion pumps in ventricular myocyte. *Biophys. J.* 81:614–629.
49. Hüser, J., L. A. Blatter, and S.-S. Sheu. 2000. Mitochondrial calcium in heart cells: beat-to-beat oscillations or slow integration of cytosolic transients? *J. Bioenerg. Biomembr.* 32:27–33.
50. Paucek, P., and M. Jaburek. 2004. Kinetics and ion specificity of Na^+/Ca^{2+} exchange mediated by the reconstituted beef heart mitochondrial Na^+/Ca^{2+} antiporter. *Biochim. Biophys. Acta.* 1659:83–91.
51. Sata, M., S. Sugiura, ..., T. Serizawa. 1996. Coupling between myosin ATPase cycle and creatinine kinase cycle facilitates cardiac actomyosin sliding in vitro. A clue to mechanical dysfunction during myocardial ischemia. *Circulation.* 93:310–317.

52. Kaasik, A., V. Veksler, ..., R. Ventura-Clapier. 2001. Energetic crosstalk between organelles: architectural integration of energy production and utilization. *Circ. Res.* 89:153–159.

53. Partikian, A., B. Ölveczky, ..., A. S. Verkman. 1998. Rapid diffusion of green fluorescent protein in the mitochondrial matrix. *J. Cell Biol.* 140:821–829.

54. Scalettar, B. A., J. R. Abney, and C. R. Hackenbrock. 1991. Dynamics, structure, and function are coupled in the mitochondrial matrix. *Proc. Natl. Acad. Sci. USA.* 88:8057–8061.

55. Olveczky, B. P., and A. S. Verkman. 1998. Monte Carlo analysis of obstructed diffusion in three dimensions: application to molecular diffusion in organelles. *Biophys. J.* 74:2722–2730.

56. Cheng, Y., Z. Yu, ..., A. P. Michailova. 2010. Numerical analysis of Ca^{2+} signaling in rat ventricular myocytes with realistic transverse-axial tubular geometry and inhibited sarcoplasmic reticulum. *PLOS Comput. Biol.* 6:e1000972.

57. Cheng, H., W. J. Lederer, and M. B. Cannell. 1993. Calcium sparks: elementary events underlying excitation-contraction coupling in heart muscle. *Science.* 262:740–744.

Displays 32 (2011) 201–208

Contents lists available at ScienceDirect

Displays

journal homepage: www.elsevier.com/locate/displa

Evaluation of temporal relationship between a physiological index and a subjective score using average mutual information

Norihiro Sugita [a,*], Makoto Yoshizawa [b], Akira Tanaka [c], Makoto Abe [b], Noriyasu Homma [b], Shigeru Chiba [d], Tomoyuki Yambe [e], Shin-ichi Nitta [e]

[a] Graduate School of Engineering, Tohoku University, 6-6-05 Aoba, Aramaki, Aoba-ku, Sendai 980-8579, Japan
[b] Information Synergy Center, Tohoku University, 6-6-05 Aoba, Aramaki, Aoba-ku, Sendai 980-8579, Japan
[c] Faculty of Symbiotic Systems Science, Fukushima University, 1 Kanayagawa, Fukushima 960-1296, Japan
[d] Sharp Corporation, 1-9-2 Nakase, Mihama-ku, Chiba 261-8520, Japan
[e] Institute of Development, Aging and Cancer, Tohoku University, 4-1 Seiryo-machi, Aoba-ku, Sendai 980-8575, Japan

ARTICLE INFO

Article history:
Available online 15 May 2011

Keywords:
Visually-induced motion sickness
Physiological index
Subjective score
Averaged mutual information

ABSTRACT

Recently, because of the ubiquitous popularization of home video cameras, countless people have had opportunities to watch video images captured by amateur cameramen. Because of this, concerns have arisen over potential negative impacts on viewer health, such as visually-induced motion sickness (VIMS). To determine the mechanism inducing VIMS and to establish a method of preventing it, it is necessary to understand which types of video scenes are associated with the onset of VIMS. Furthermore, while it is useful to consider viewer self-assessments while watching such scenes, physiological indices can provide even more information because they can be measured second-by-second in real time. However, there is not much knowledge regarding the temporal relationships between the severity of VIMS and its accompanying physiological conditions. In this study, the average mutual information was employed to determine the temporal relationship between subjective evaluation scores (a subject's personal evaluation of his/her own condition) and various physiological indices present when people suffer from VIMS. Our analysis of experimental data found that changes in the two physiological indices, which were respiratory sinus arrhythmia and the maximum cross-correlation coefficient between heart rate and pulse transmission time, had a concordance rate of more than 60% with changes in the severity of VIMS symptoms experienced by test subjects. Furthermore, we determined that it may be possible to detect signs of impending VIMS prior to the development of symptoms by analyzing physiological indices.

1. Introduction

In recent years, countless people have seen moving video images taken by amateur videographers. As a consequence, video cameras have become significantly less expensive and because the popular trend of posting private videos on the Internet has expanded exponentially. Concurrently, the number of cases reported in which viewers suffered from visually-induced motion sickness (VIMS) during or after watching a video, including unexpected whole image motion and vibration [1–9], has increased. VIMS is a form of motion sickness that does not require the subject to experience motion. However, VIMS symptoms are similar to those of other motion sicknesses. Most notably, such symptoms include skin pallor, excessive perspiration, nausea, and vomiting. At a junior high school in Japan on July 10, 2003, an incident occurred in which 36 of 294 students were treated in a hospital after complaining of dizziness and nausea induced by watching a video taken by an amateur videographer with a swaying handheld camera [6]. Furthermore, several film distributors and video game producers have recently issued warnings to viewers or users about the possibility of experiencing VIMS from watching their videos or playing their games: a movie titled "Clover Field" released in 2008 was one such example.

A number of *hypotheses* and discussions about the pathogenesis of various forms of motion sickness, including VIMS [10–12], have been explored. Nevertheless, there is currently little understanding about adverse effects of VIMS on the human body. Accordingly, sufficient attention should be focused on dealing with moving images and scenes that have potential to induce VIMS, especially in the case of children, because their nervous systems are immature.

To isolate the VIMS induction mechanism and to establish a method of preventing it, it is important to understand which

* Corresponding author. Tel.: +81 22 7957130; fax: +81 22 2639163.
E-mail address: sugita@yoshizawa.ecei.tohoku.ac.jp (N. Sugita).

0141-9382/$ - see front matter © 2011 Elsevier B.V. All rights reserved.
doi:10.1016/j.displa.2011.04.003

scenes in a video are associated with the onset of VIMS. Self-assessment of VIMS by subjects at regular intervals is considered to be one of the most effective methods of detecting these scenes. In particular, Kennedy developed the Simulator Sickness Questionnaire (SSQ) [13] which has been used in many studies [14–17]. The SSQ contains 16 items to check the subject's physical disorder. The subject rates the degree of these items in four levels. Three subscales, i.e., nausea, oculomotor, and disorientation, are calculated on the basis of these items, and a total score is calculated with these subscales. In these scales, the nausea subscale or the total score is considered to be useful for evaluating the severity of VIMS. However, since SSQ results can normally only be obtained after a subject has watched a video, it is difficult to follow changes in VIMS severity over time. Furthermore, even if self-assessment is accomplished using an easier reporting method than SSQ, such as reporting symptoms via keyboard input or verbally, the very act of making such reports has the potential to distract subjects from the scene they are viewing, and thus modify the VIMS development.

In contrast, other previous studies [2–5,7,8,18–23] have reported that real-time monitoring of physiological indices is also useful for detecting and following the development of VIMS. Specifically, skin conductance [20,21] and gastric tachyarrhythmia [2,20,22] are considered to be particularly indicative of possible VIMS. Furthermore, physiological indices based on heart rate variability (HRV) such as variations in respiratory sinus arrhythmia (RSA) [10,11] have possibilities of detecting the development of VIMS. The indices obtained from HRV are associated with autonomic nervous activity. Fig. 1 shows an example of the power spectrum density of HRV. In this figure, the high frequency component corresponding to RSA includes parasympathetic nervous activity only while the low frequency component (LF_{HRV}) includes both sympathetic and parasympathetic nervous activities [24,25]. These physiological indices are susceptible to change when a person experiences VIMS because VIMS is considered to be a kind of the physical and emotional stress which disturbs autonomic nervous balance. We previously proposed a maximum cross-correlation coefficient (ρ_{max}) between heart rate and blood pressure and reported that this index decreased significantly when people suffered from VIMS [4]. ρ_{max} is considered to reflect baroreflex function which is influenced by autonomic nervous activity [26–28]. In addition, ρ_{max} which was calculated using pulse transmission time (PTT) [29] instead of blood pressure was also found to be useful when evaluating VIMS effects [3,5].

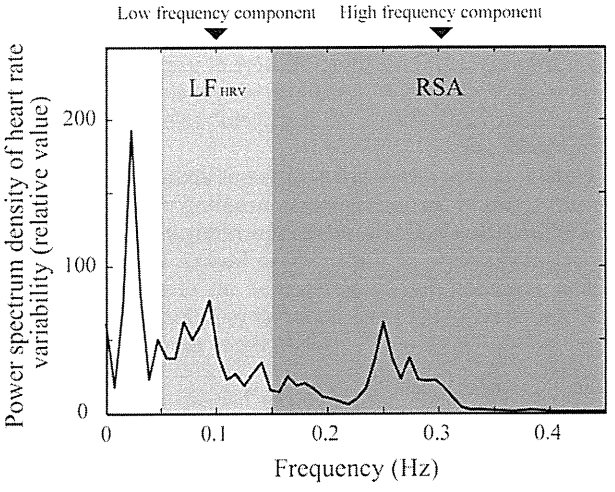

Fig. 1. The power spectrum density of heart rate variability.

Information on the abovementioned physiological indices can be obtained in real-time using non-invasive sensors while the subjects are watching a video, which makes it possible to compare changes in these indices with particular video scenes and thus observe the process of VIMS onset with relatively little effect on the subjects. However, one problem identified is that biological reaction times, especially response times, vary between individuals. Meanwhile, there have been few studies into the temporal relationship between the development of VIMS as evaluated by subjective scores and by the physiological responses of the subjects [19].

In this study, we hypothesize that there is no significant difference between the time when subjects experience VIMS symptoms and the time when their physiological states change. To test this hypothesis, an experiment was conducted to investigate the temporal relationship between a subjective score and four physiological indices, HRV, LF_{HRV}, RSA, and ρ_{max}, from subjects experiencing VIMS. It was not clear whether HRV and LF_{HRV} reflect the development of VIMS, although RSA and ρ_{max} were reported to have relationships with VIMS in previous works [3–5,18,19].

2. Methods

2.1. Experimental design

In the experimental phase of this study, both subjective scores and biological signals were measured simultaneously while subjects were watching a video. The test subjects evaluated the degrees of VIMS they experienced at regular intervals using a joystick. In contrast, physiological state changes, HRV, LF_{HRV}, RSA, and ρ_{max} using PTT were obtained via biological signals, and were used as physiological indices to test our hypothesis. Furthermore, we proposed a new evaluation indicator, which will be described in detail later, to investigate the temporal relationship between subjective scores and the physiological indices.

The experimental protocol was approved by the University's Internal Review Board.

2.2. Participants

Fifty-one adults (22 males and 29 females; 26.6 ± 9.3 years) participated in the experiment. They were recruited via posted announcements on university notice boards, and all of them received payment for their participation in the experiment.

Informed consent was obtained from each of the subjects and each was asked about their backgrounds and health conditions through a questionnaire. The results of the questionnaire showed that there were no test subjects whose participation in the experiment would be unsuitable due to health issues.

2.3. Stimulus

The subjects watched a 20-min-long amateur video that included three segments, as shown in Fig. 2. Segment one consisted of moving images taken by a young girl using a hand-held camera while strolling around an urban area. Therefore, the video contained numerous scenes that included unexpected whole image motions and vibration. The images of Segment 2 were taken in an amusement park. Thus, the camera movements were sometimes intense due to the movements of the theme-park rides. Segment 3 includes images of a young woman strolling around a city, recorded normally, and using four simple camera motions: tilt, pan, roll and zoom. Before and after these segments, a gray, imageless screen display was presented to the subjects for 5 min 30 s and 2 min, respectively. Therefore, each subject watched a total of 27 min 30 s of video during the experiment. None of the three vi-

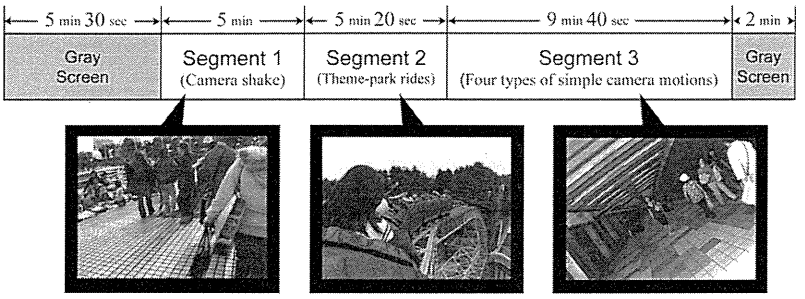

Fig. 2. Overview of the video presented to experimental subjects.

deo segments had story lines and there were no violent scenes that might induce emotional effects.

The global motion vectors (GMVs) of the video are shown in Fig. 6a). GMVs are measurements of deviation between consecutive frames and represent degrees of motions in four axes: pan, tilt, roll and zoom. A detailed description of the method used for estimating GMVs is provided in Ref. [30]. As shown in Fig. 6a, scenes with intense camera movements and those without were mixed in the video on purpose to induce ups and downs of VIMS symptoms.

2.4. Equipment

The video was shown on a 37-in. liquid crystal display (resolution: 1920 × 1080 pixels, maximum brightness: 200 cd/m^2). The experimental room had curtains that eliminated all outside light and illumination intensity was maintained at approximately 50 l×. The room temperature was controlled with an air conditioner to be approximately 22 °C.

During the experiment, an electrocardiogram (ECG) for RSA, PTT, and HRV was measured using electrodes placed on the subjects chests. In addition, a finger photoplethysmogram (PPG) for PTT was also measured using a photoplethysmographic sensor attached on their finger tips, as shown in Fig. 3. These signals were amplified and recorded by a data acquisition system (MP-100, ECG100C, PPG100C; BIOPAC System Inc.); whose voltage resolution and sampling rate were 16 bit and 1 kHz, respectively.

2.5. Procedure

The subjects were instructed not to engage in intense physical activity and to avoid eating anything for 2 h prior to the experiment.

First, each subject was asked to complete a questionnaire about their background and health condition. Additionally, an SSQ [13] was administered before and after the experimental task to measure their VIMS symptoms. Next, after being seated in the room and given 10 min to adapt to the darkness, they began viewing the video.

While watching the video, test subjects sat on a chair placed 70 cm away from the display with a 60.5 × 40.3° field of view, and they rated the level of nausea they felt on a scale of zero to three by moving a joystick, as shown in Fig. 4. The number of symptom levels was limited to four and enough time for practice was given to the subjects before the experiment so that they could move the joystick appropriately without looking at it. A buzzer was sounded at 1 min intervals to let the subjects know it was time to rate their nausea level.

2.6. Data analysis

There were five subjects who complained of VIMS symptoms that were so severe that they could not continue to watch the video. All these subjects experienced nausea and had unnatural skin pallor. One female test subject developed an erratic heartbeat just before the experiment was stopped. Additionally, test data from 17 other subjects were excluded from the analysis because of artifacts. There were a large number of subjects whose photoplethysmogram signals contained artifacts caused by body movements. As shown in Fig. 3, the photoplethysmographic sensor is attached to the skin on a finger of a subject and detects infrared light modulated by blood pulsing through the tissue below. Therefore, the photoplethysmogram signal is disturbed if the subject's upper body including fingers moves much. Furthermore, data from another six subjects whose subjective scores were zero through the video were also excluded from the analysis. The reason of this will be discussed later. As a result, only the data of 23 subjects (10 males and 13 females; 27.6 ± 10.0 years) were analyzed.

As previously mentioned, we proposed a new evaluation indicator to investigate the temporal relationship between subjective

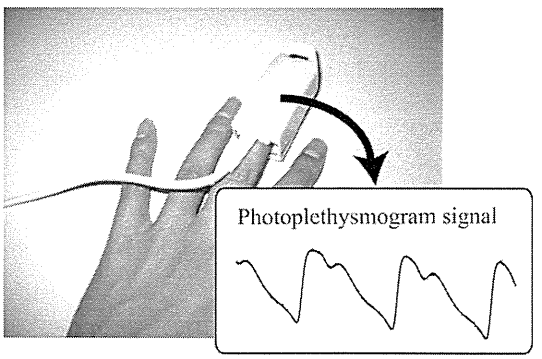

Fig. 3. Photoplethysmographic sensor attached on a subject's finger tips.

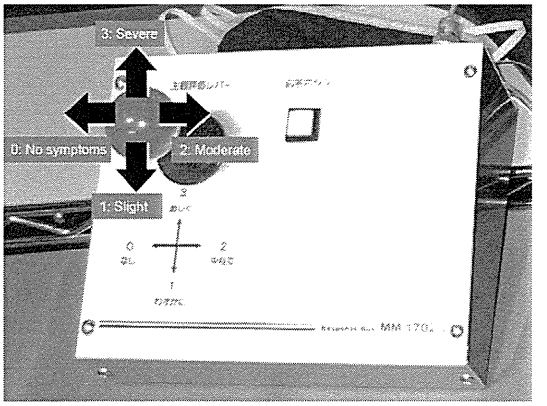

Fig. 4. Joystick used by subjects to rate VIMS symptoms during the experiment.

scores and physiological indices. In concrete terms, the average mutual information (AMI) [31] was calculated to measure the statistical dependence between the two. The AMI between two variables shows how frequently, on average, one of them can be estimated from the other. Thus, by introducing the AMI, it is possible to estimate the statistical dependence correctly even if the relationship between the variables is not linear. This property is important because our understanding of the linearity between subjective scores and physiological indices is still poor.

Problems sometimes occurred when calculating the AMI between subjective scores and physiological indices. Specifically, not only is the difference in the numeric resolution between them large, but the pattern of their changes differs significantly between individual subjects. To solve these problems, the AMI was calculated as the statistical dependence between events defined by changing patterns of variables, which were assessed as increasing, decreasing or stable.

We will further illustrate this point with an example utilizing two test subjects. In this example, when the subjective scores of the two subjects increase, the physiological index of one subject always increases while that of the other always decreases, and vice versa. In this situation, a difference appears in the value of an AMI calculated directly from the physiological index and the subjective scores of the two subjects. In contrast, the value of an AMI calculated based on events defined by changing patterns of the physiological index and the subjective scores of the two subjects is the same. Types of VIMS symptoms should differ among subjects, for example, eye fatigue, a headache or stomach discomfort. And autonomic nervous activities are supposed to vary in these different symptoms. For this reason, it is no wonder if directions of the change in physiological indices differ among the subjects when they suffered from VIMS. Additionally, the problem caused by the numerical differences between the two variables is also eliminated by simply comparing their changing patterns.

The method used to calculate the AMI will now be described in detail. First, events A_1, A_2, A_3 and B_1, B_2, B_3 are defined as follows:

$$\begin{aligned} A_1 &\Longleftrightarrow SS(k) - SS(k-1) > 0 \\ A_2 &\Longleftrightarrow SS(k) - SS(k-1) = 0 \\ A_3 &\Longleftrightarrow SS(k) - SS(k-1) < 0 \end{aligned} \tag{1}$$

$$\begin{aligned} B_1 &\Longleftrightarrow \frac{PS(k)}{PS(k-1)} > 1 + Tr \\ B2 &\Longleftrightarrow 1 - Tr < \frac{PS(k)}{PS(k-1)} \leqslant 1 + Tr \\ B3 &\Longleftrightarrow \frac{PS(k)}{PS(k-1)} \leqslant 1 - Tr \end{aligned} \tag{2}$$

where $SS(k)$ and $PS(k)$ are the subjective score and the physiological index at a given time k, respectively, and Tr is the threshold. A method to determine Tr is described later.

Next, the AMI between A_i and B_j (i, $j = 1,2,3$) is defined as follows:

$$I(A_i; B_j) = -\sum_{i=1}^{3} P(A_i)\log_2 P(A_i) + \sum_{i=1}^{3}\sum_{j=1}^{3} P(A_i, B_j)\log_2 P(A_i|B_j) \tag{3}$$

where $P(A_i)$ is the occurrence probability of A_i, $P(A_i, B_j)$ is the joint probability of A_i and B_j, and $P(A_i|B_j)$ is the conditional probability of A_i assuming that B_j has occurred.

By its nature, I between arbitrary variables X and Y does not contain directional information. In other words, I does not show causality between X and Y, although it is possible to detect causality between X and Y by the calculation of I using X_L instead of X. X_L is the time series which lags X by L [32]. That is, I between $SS(k)$ and $PS(k + L)$, which is denoted as $I(L)$, shows how much time lag or lead there is between physiological and psychological state changes. $I(L)$ was calculated under lag time set from $L = -2$ to 2 min.

To determine the value of the threshold Tr in equation (2), an assessment function $H(Tr)$ is defined as follows:

$$H(Tr) = \max_{-2 \leqslant L \leqslant 2} I(L) \tag{4}$$

For each subject, the value of Tr was selected to maximize $H(Tr)$ in the range from $Tr = 0.01$ to 0.15.

In this study, the subjective score obtained from the joystick input was chosen as $SS(k)$. Meanwhile, time series of ρ_{max} using PTT, RSA, HRV and LF_{HRV} were chosen as $PS(k)$.

In order to obtain time series of these parameters, beat-to-beat data of HRV and PTT were first calculated. The HRV was calculated from the reciprocal of the inter-R-wave interval of ECG signal and the PTT was defined as the interval from the peak of ECG, R-wave, to the point at which PPG signal begins to rise. And then, at a given time k (min), $\rho_{max}(k)$ was calculated based on the HRV and the PTT observed in the interval between $k - 1$ and k (min). A detailed description of the calculation method of ρ_{max} is provided in Ref. [5]. Similarly, $HRV(k)$, $LF_{HRV}(k)$ and $RSA(k)$ were calculated as the mean value, the low-frequency power (0.05–0.15 Hz) and the high-frequency power (0.15–0.45 Hz) of HRV, respectively, in the same interval as described above.

3. Results

Fig. 5 shows the results of the SSQ completed by the subjects before and after the experiment. In these results, all SSQ scores increased significantly ($p < 0.01$, paired t-test) after watching the video and got closer to those obtained from the subjects who were suffered from cyber sickness or simulator sickness [14,23]. Therefore, the moving images included in the video are considered to have induced VIMS.

Fig. 6b shows the changes in ρ_{max} and SS of a subject. SS increased at 11, 15, 20, 24 and 26 min, while ρ_{max} decreased at approximately the same points of time (except for the 24 min point). Fig. 6c shows the average mutual information I between SS and ρ_{max} of this subject. In this figure, I at $L = 0$ min was higher than those observed at the other lag times. This result indicates that the subject's physiological state changed at approximately the same time a VIMS sensation was experienced.

From Fig. 6c, I had a value of 0.3 at $L = 0$. However, the meaning of this value is unclear. Therefore, a computer simulation was carried out to investigate the relationship between I and the concor-

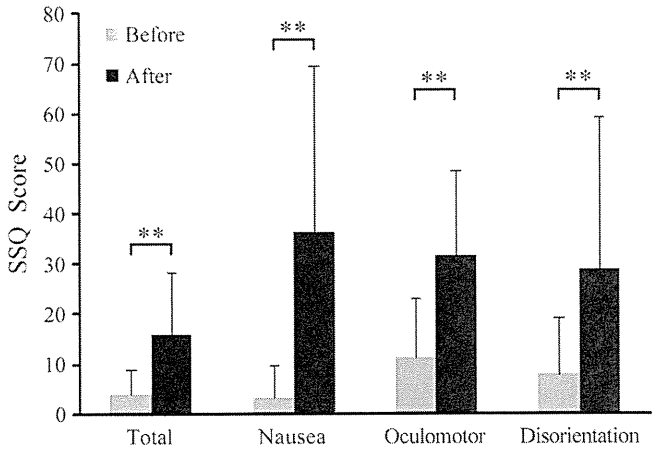

Fig. 5. SSQ scores obtained from subjects before and after watching the video. $^{**}p < 0.01$, paired t-test.

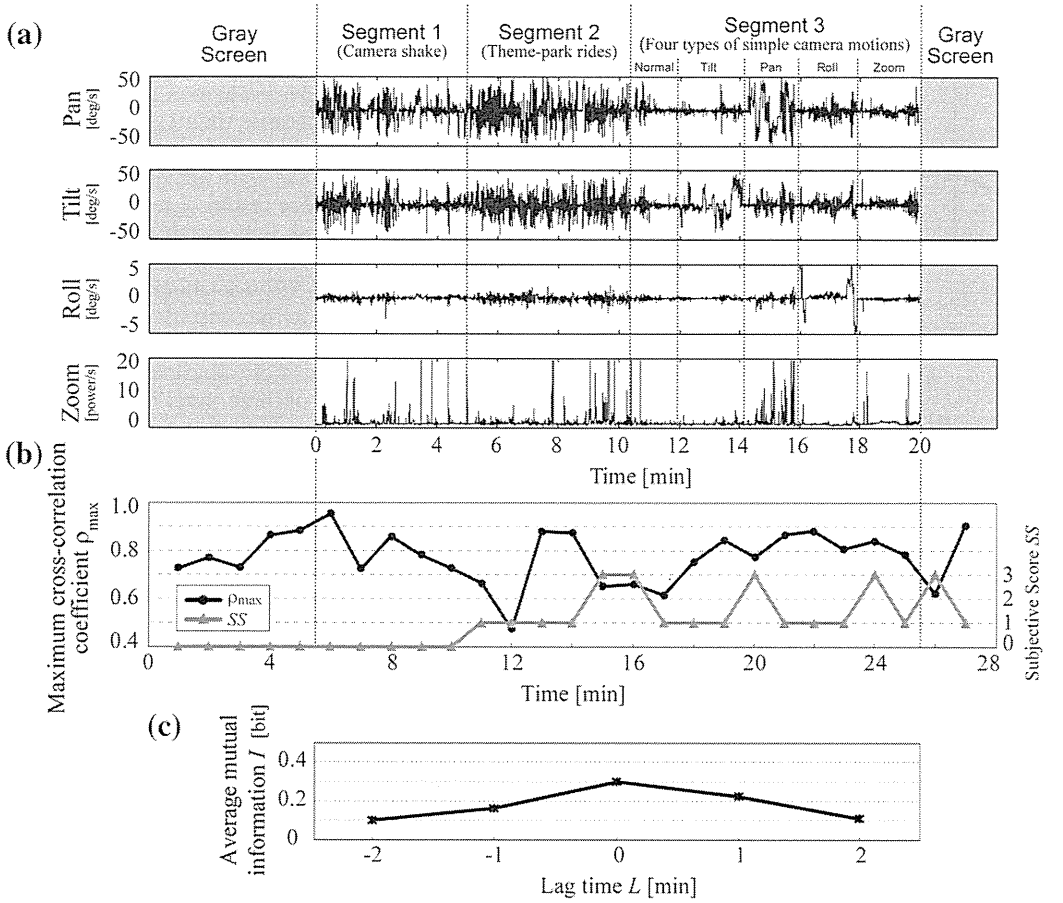

Fig. 6. (a) The global motion vectors of the self-produced video, (b) changes in ρ_{max} (black line) and *SS* (gray line) of a subject, and (c) average mutual information *I* between the *SS* and the ρ_{max}.

dance rate p_c of changing patterns of two temporal sequences resembling *SS*(k) and *PS*(k). In the simulation, these temporal sequences changed in the same direction at a rate of p_c (%) and did so in random directions at a rate of 100 – p_c (%).

Fig. 7 shows the simulation results. The curve shown in the figure was obtained from a simulation that was performed 1000 times. It can be seen that *I* had a minimum value when p_c was about 33%. This is because there were only three events defined by the difference in the changing pattern of temporal sequences, as shown in Eqs. (1) and (2). Therefore, even if changes to these temporal sequences are perfectly random and there is no statistical dependence between them, they change in the same direction, at a minimum, 33% of the time. This result implies that it is meaningless to compare the values of *I* which are lower than 0.15. In addition, there was a tendency in *I* to increase as p_c decreases when p_c was lower than 33%. This is because the occurrence of two temporal sequences whose changing patterns are significantly different to each other is extremely unlikely to be coincidental.

Fig. 8 shows the mean values of *I* between *SS* and ρ_{max}. These values were calculated as the mean of all test subjects with respect to each lag time between $L = -2$ and 2 min. The values of *I* at $L = -2$ and 2 min showed a lower level than those at the other lag times. However, the standard deviation of *I*, which means individual differences, was high for all lag times. In Fig. 9, relationships between lag time and *I* were plotted for all the subjects whose *I* were the highest at $L = -1$ or 1, hereinafter referred to as $L_{max} = -1$ or 1, respectively. As shown in this figure, there is a possibility that each subject has his/her specific L_{max} because there is only one peak in *I* of each subject for all lag times. And the values of *I* were less than

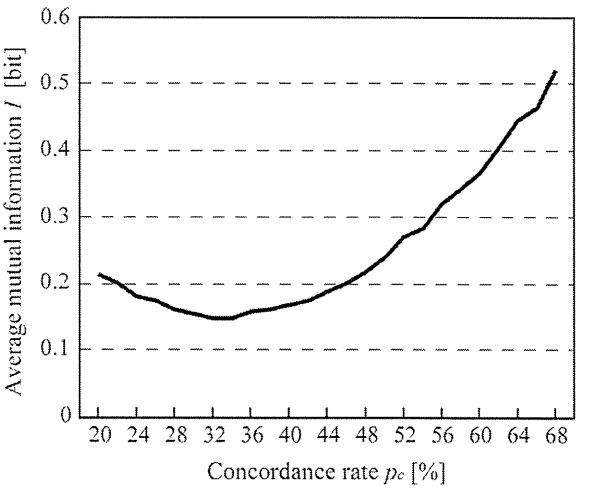

Fig. 7. Relationship between average mutual information *I* and the concordance rate p_c of changes in temporal sequences resembling *SS*(k) and *PS*(k). This is the simulation result.

0.2 at other lag times than L_{max}, which indicates there is no statistical dependence between *PS* and *SS*. Thus, for example, if the number of subjects whose L_{max} were −1 increases, the mean value of *I* at $L = 1$ will be relatively low.

To investigate not only the distribution but also the mean value of *I* for subjects with different L_{max}, the mean value of *I* at a lag time L_0 was only calculated for subjects whose L_{max} were L_0. For exam-